# Chapter 5

# Hydrogen diffusion in potassium-intercalated graphite

## 5.1 Introduction

Hydrogen is adsorbed in large amounts by $KC_{24}$ at low temperatures. The potassiums, hydrogens and vacancies essentially form a two-dimensional ternary lattice gas between the host graphitic layers. Due to the ionized metal atoms and the overlapping graphite corrugation potentials, adsorbed $H_2$ molecules experience a strong anisotropic potential. This provides an opportunity to study both the effect of steric barriers and strong binding interactions on the diffusion of the adsorbed $H_2$ molecules. As an indicator of macroscopic transport behavior, we know that hydrogen adsorption in $KC_{24}$ is kinetically-limited at large fillings (see Sec. 4.4). In this chapter, the microscopic self-diffusion of hydrogen in $KC_{24}$ is investigated using quasielastic neutron scattering (QENS) and molecular dynamics simulations. Neutron scattering is an experimental technique particularly well-suited to quantitatively studying the molecular motions of hydrogen (and other hydrogen-rich fluids) adsorbed in host frameworks. It also provides a unique opportunity to directly compare the simulated and experimental values of fluid diffusivities at the microscopic level.

Portions of this chapter were published in the article: J. J. Purewal, J. B. Keith, C. C. Ahn, C. M. Brown, M. Tyagi and B. Fultz, *Phys. Rev. B* **2009**, *79*, p. 054305.

## 5.2 Quasielastic neutron scattering

### 5.2.1 Description

Quasielastic scattering is a broadening of final neutron energies caused by the diffusion of atoms within a material. Consider an atom which jumps to a new lattice site before it completes the scattering of a neutron wavepacket. It will continue to scatter the neutron wavepacket from its new position. In "quasielastic" scattering the neutron does not cause transitions between the quantum states of the target material. The two scattered waves will typically interfere destructively (unless of course the initial and final positions are separated by an arbitrary fraction of the neutron wavelength). The uncertainty principle tells us that $\Delta E = \hbar/\Delta t$, where $\Delta t$ is the average time that an atom resides on a particular site. The final neutron energies are symmetrically broadened around $\Delta E = 0$ due to the uncertainty in $\Delta t$. Based on this idea, quasielastic scattering can be used to measure the time scale of the diffusive jumps. Spectrometers can currently measure quasielastic broadening over an energy range of 1 μeV to 1 meV, which corresponds to characteristic jump times of $10^{-9}$ s to $10^{-12}$ s. When diffusion occurs on a fixed sublattice the quasielastic scattering can exhibit a $Q$-dependence which provides information on the geometry of the diffusive jumps.

### 5.2.2 Continuous diffusion

The simplest model for long-range diffusion is isotropic, three-dimensional, continuous diffusion. The starting profile at $t = 0$ is a delta function, and at finite time it is a Gaussian in $\mathbf{r}$. The variation of the Gaussian distribution of molecular displacements gives a mean-squared displacement of $\langle r^2 \rangle = 6Dt$, where $D$ is the self-diffusion coefficient. As described

in Sec. 3.2.2, the incoherent scattering function is the Fourier transform in time and space of the van Hove autocorrelation function. Vineyard [83] calculated the incoherent scattering function for this system,

$$S_{\mathrm{inc}}(\mathbf{Q},\omega) = \frac{1}{\pi}\frac{DQ^2}{\left(DQ^2\right)^2 + \omega^2}, \tag{5.1}$$

which is a Lorentzian with a width (HWHM) of $\Gamma = DQ^2$. This law is typically valid at small $Q$, where distances are large compared with the individual steps of the diffusion process. Large deviations from the $\Gamma = DQ^2$ behavior is observed at large $Q$, however, where underlying jump mechanism becomes important.

When the continuous diffusion is two-dimensional (such as between the graphite planes in $KC_{24}$) the limiting form of the scattering function assumes the following form,

$$S^{\mathrm{2D}}_{\mathrm{inc}}(\mathbf{Q},\omega) = \frac{1}{\pi}\frac{D_{\mathrm{2D}}\left(Q\sin\theta\right)^2}{\left[D_{\mathrm{2D}}\left(Q\sin\theta\right)^2\right]^2 + \omega^2}, \tag{5.2}$$

where $D_{\mathrm{2D}}$ is the self-diffusion in two dimensions, and $\theta$ is the angle that the normal to the diffusion plane makes with $\mathbf{Q}$ [84]. This model predicts that elastic scattering is obtained when $\mathbf{Q}$ is perpendicular to the diffusion plane (i.e., $\theta = 0$). Lorentzians of increasing width are obtained as $\theta$ increases. The powder-averaged scattering function then has a cusp-like shape with a logarithmic singularity at $\omega = 0$. This is illustrated in Fig. 5.1. For continuous diffusion in a general lamellar system of arbitrary width, the scattering function is actually an infinite sum of Lorentzians with $Q$-dependent amplitudes [85].

### 5.2.3 Jump diffusion

A jump diffusion model takes into account the microscopic diffusive steps and therefore provides more accurate predictions at large $Q$. The standard model for jump diffusion is

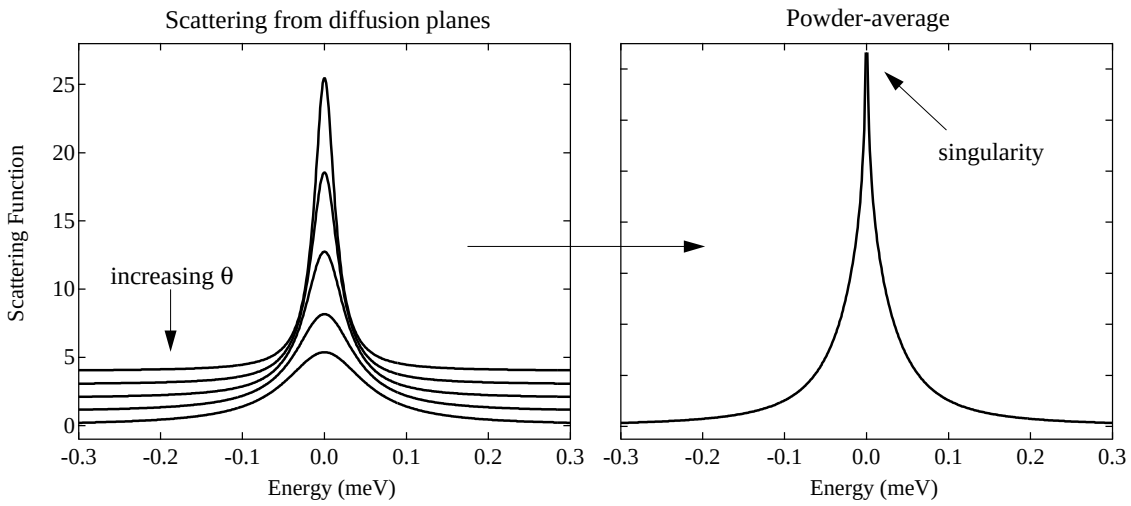


**Figure 5.1:** Left: Scattering functions for continuous two-dimensional diffusion. The angle $\theta$ between the diffusion plane normal and $\mathbf{Q}$ increases going down the set of curves. Right: Scattering function obtained by taking a powder average over all orientations.

the *Chudley-Elliott* model [86]. This model assumes that the sublattice on which diffusion occurs is a Bravais lattice and that successive jumps are uncorrelated. The latter assumption means that the model is only valid in the dilute limit where correlation effects are absent. The particle stays at a site for a mean residence time $\tau$ and jumps to one of its $z$ nearest-neighbor sites. There are then a set of $z$ possible jump vectors, which are denoted $\{\mathbf{l}_i\}$. The scattering function can be calculated as

$$S_{\mathrm{inc}}(\mathbf{Q},\omega) = \frac{1}{\pi}\frac{|\Gamma(\mathbf{Q})|}{|\Gamma(\mathbf{Q})|^2 + (\hbar\omega)^2}, \tag{5.3}$$

where the peak width is given by

$$\Gamma(\mathbf{Q}) = \frac{\hbar}{z\tau}\sum_{j=1}^{z}\left(1 - e^{-i\mathbf{Q}\cdot\mathbf{l}_j}\right). \tag{5.4}$$

In the low-$Q$ limit, it reduces to the continuous diffusion form $\Gamma = \hbar D Q^2$, with $D = l^2/6\tau$. The peak-shape is Lorentzian with a width that varies sinusoidally depending on the

sublattice geometry. This model can be extended to a non-Bravais lattice, as described in Ref. [87]. In this case the scattering function contains a sum of $m$ weighted Lorentzians, where $m$ is the number of inequivalent sites in the unit cell.

### 5.2.4 Concentration effects

For a finite concentration, equal to $c$, there are correlations between successive jumps on the sublattice. After a single jump, a particle has an increased probability of jumping back to its initial (now unoccupied) site compared to a jump to other nearest-neighbor sites (which are occupied with probability $c$). In the mean-field approximation, we can simply adjust the mean residence time to allow for site-blocking:

$$\tau(c) = \frac{\tau(0)}{1-c}. \tag{5.5}$$

The scattering function is still a Lorentzian but now with a width that has been corrected by a site-blocking factor. If we also consider memory effects due to correlation between successive jumps, then the effective self-diffusion coefficient has a concentration-dependent expression

$$D = \frac{f(c)l^2}{\tau(c)}, \tag{5.6}$$

where $f(c)$ is the tracer correlation factor for long-range diffusion. There have been a number of studies to determine whether $S_{\mathrm{inc}}(Q,\omega)$ at high concentrations can still be described by a Lorentzian with a width corresponding to the effective diffusivity (Eq. 5.6). The results seem to depend both on the computational method and on the assumptions made [88]. Nevertheless, the jump diffusion model should not be applied at high concentrations.

## 5.3 Experimental methods

Neutron scattering measurements were performed on the Disc Chopper Spectrometer (DCS) at the NIST Center for Neutron Research [81]. For the current measurements, a $KC_{24}$ sample with a mass of approximately 2.2506 g was transferred in a high-purity helium glovebox to an annular-geometry aluminum sample cell, sealed with an indium o-ring. The sample thickness was chosen for 10% total scattering. The sample can was mounted onto a sample stick which was adapted for a top-loading, closed-cycle helium refrigerator system. The sample can was connected with a stainless steel capillary line to a gas handling rig containing a calibrated volume and a high resolution pressure transducer. Hydrogen loading was performed at 60 K by filling the calibrated volume with the precise amount of $H_2$ gas needed for a $KC_{24}(H_2)_{0.5}$ composition, opening the valve to the sample, and monitoring the pressure as it dropped to approximately 0 Torr.

Scattering from bare $KC_{24}$ was measured at 40 K and 60 K on DCS. The neutron scattering spectra at the different temperatures were identical within the instrument resolution. Scattering from $KC_{24}(H_2)_{0.5}$ was collected at 80 K, 90 K, 100 K, and 110 K. By monitoring the pressure, we confirmed that there was not any significant desorption of $H_2$ at these temperatures. Since the incoherent scattering cross-section of hydrogen is very large, approximately 35 % of the total scattering is from hydrogen. The background signal from $KC_{24}$ is subtracted to isolate the scattering from hydrogen alone. Diffraction peaks from the host $KC_{24}$ material are a significant feature in the $S(Q, \omega)$. Because the metal-containing graphite galleries expand approximately 5% upon $H_2$ adsorption, the $KC_{24}$ diffraction peaks shift to slightly lower $Q$ values, causing the $KC_{24}$ background to over-subtract on the high $Q$ side. Therefore it is necessary to mask the detector banks containing the diffraction peaks in

both the $KC_{24}$ and $KC_{24}(H_2)_{0.5}$ samples. To improve statistics and make up for missing data in the masked detector groups, the reduced $S(Q,\omega)$ was binned into momentum-transfer increments of $0.15\,\text{Å}^{-1}$ and into energy increments of $0.01\,\text{meV}$ .

The DCS measurements in this chapter were collected using an incident neutron wavelength of $\lambda = 6.0\,\text{Å}$, operating the choppers in low resolution mode, with a speed ratio of 2/3, a sample-detector minimum time of 500, and a master speed of 20 000 rpm. These settings give an energy resolution of approximately $65\,\mu\text{eV}$ at the elastic line. The kinematically-allowed region includes a maximum neutron energy loss of $1.35\,\text{meV}$, and a wavevector transfer between $0.1\,\text{Å}^{-1}$ to $2.0\,\text{Å}^{-1}$.

## 5.4 Quasielastic scattering results

An example of the QENS spectra of $KC_{24}(H_2)_{0.5}$ measured on DCS is shown in Fig. 5.2. The instrument resolution is plotted as a dashed red line. A low concentration ($x = 0.5$) was used for these measurements in order to minimize the effects of correlation and site-blocking. The QENS spectra consist entirely of scattering from $H_2$ since the signal from bare $KC_{24}$ was subtracted as a background. There is a considerable amount of quasielastic line broadening due to the diffusion of adsorbed $H_2$ molecules. At $80\,\text{K}$, the spectrum contains both a broad quasielastic component and a sharp elastic component. Elastic scattering can originate from either the geometry of the hydrogen diffusion, or from a population of $H_2$ molecules whose motions are too slow to be resolved by the instrument. The intensity from the elastic component decreases with temperature, and is fairly small at $110\,\text{K}$. Since the amount of hydrogen was confirmed to be constant in all of the spectra, the decrease in total intensity is simply due to a decrease in elastic scattering at higher temperatures (i.e., the Debye-Waller factor). To obtain information from the QENS spectra about the diffusion

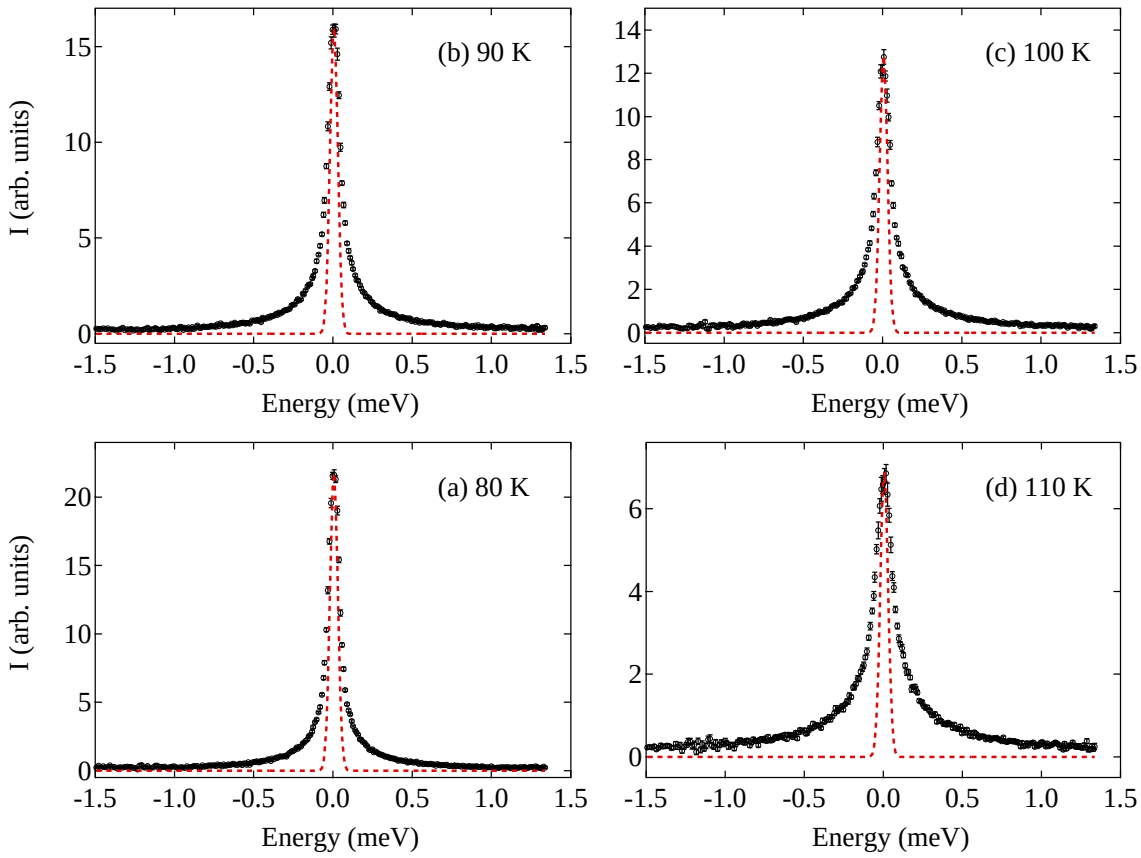


**Figure 5.2:** QENS scattering of $KC_{24}(H_2)_{0.5}$ at $Q = 1.61\,\text{Å}^{-1}$ measured on DCS with wavelength $\lambda = 6\,\text{Å}$, after subtracting scattering from bare $KC_{24}$. Dashed red lines indicate instrument resolution.

mechanism, it is necessary to develop a detailed jump diffusion model and then fit it to the experimental data. This is done in the next section.

## 5.5 Honeycomb lattice diffusion model

In a first approximation the diffusion of $H_2$ molecules in $KC_{24}$ is two-dimensional. It is unlikely that the hydrogen will pass through two graphite planes into the neighboring intercalate layers (if it does happen it will be on a vastly slower time scale than in-plane diffusion). We assume that the $\left(\sqrt{7} \times \sqrt{7}\right) R\,19.11°$ structure adequately describes the in-plane structure of $KC_{24}$ at low temperature. As depicted in Fig. 5.3, the sublattice of $H_2$

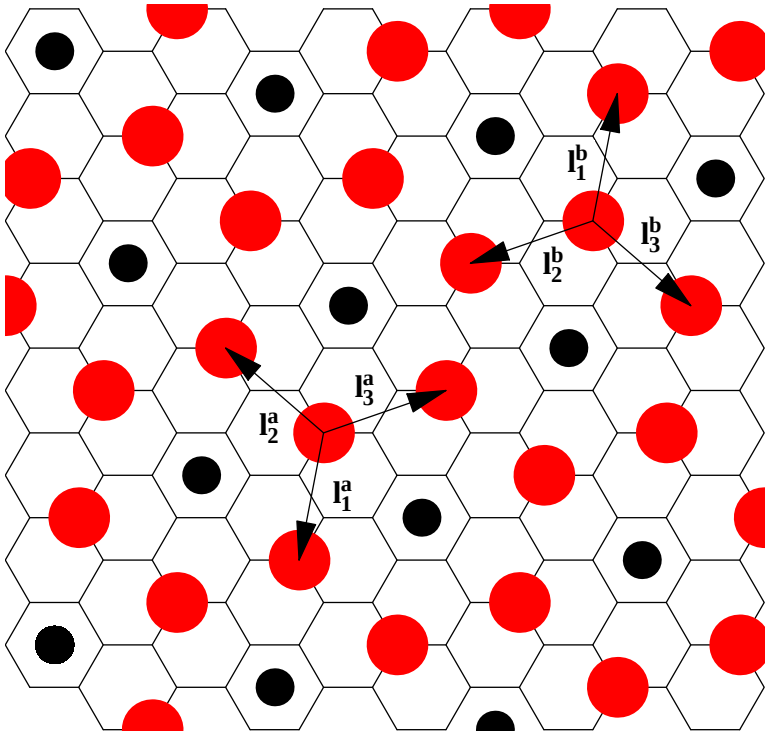


**Figure 5.3:** Hydrogen sorption sites in a $\left(\sqrt{7}\times\sqrt{7}\right) R19.11^\circ$ structure. The sorption sites form a 2D honeycomb net. Potassiums are represented by black dots while hydrogen sorption sites are represented by red dots. Sets of jump vectors for the two non-equivalent basis points are labeled $\{\mathbf{l}_i^a\}$ and $\{\mathbf{l}_i^b\}$. The length of each jump vector is 3.7 Å.

sorption sites forms a honeycomb net, which is *not* a Bravais lattice. The primitive unit cell contains a basis of two nonequivalent sites, and thus there are two distinct sets of jump vectors $\{\mathbf{l}_1^a, \mathbf{l}_2^a, \mathbf{l}_3^a\}$ and $\{\mathbf{l}_1^b, \mathbf{l}_2^b, \mathbf{l}_3^b\}$.[1] In calculating the scattering function, we assume that $\tau$ is the mean residence time of $H_2$ molecules on the honeycomb sublattice sites, and also assume that there is no correlation between consecutive jumps. The honeycomb lattice has a basis of two lattice points, and the scattering function is calculated using the procedure described in Ref. [87]. The result of these calculations is a sum of two Lorentzians [89],

$$S_{\text{inc}}(\mathbf{Q},\omega) = \frac{1}{\pi}\sum_{j=1}^{2}\frac{w_j(\mathbf{Q})\Gamma_j(\mathbf{Q})}{\omega^2+\Gamma_j^2(\mathbf{Q})}, \tag{5.7}$$

[1]The fact that the $\{\mathbf{l}_i^a\}$ jump vectors are simply the negative of the $\{\mathbf{l}_i^b\}$ jump vectors is implicitly included in the remainder of the calculation. Therefore only one set of jump vectors will be referenced in the derivation in this section.

where the weights $w_j(\mathbf{Q})$ and linewidths $\Gamma_j(\mathbf{Q})$ of the two Lorentzians are given by

$$w_1(\mathbf{Q}) = \tfrac{1}{2}\left(1 + \mathrm{Re}(\mathbf{K})/|\mathbf{K}|\right) \qquad w_2(\mathbf{Q}) = \tfrac{1}{2}\left(1 - \mathrm{Re}(\mathbf{K})/|\mathbf{K}|\right) \tag{5.8}$$

$$\Gamma_1(\mathbf{Q}) = L - |\mathbf{K}| \qquad \Gamma_2(\mathbf{Q}) = L + |\mathbf{K}| \tag{5.9}$$

and values of $L$ and $\mathbf{K}$ are given by

$$L = \frac{1}{\tau} \qquad \mathbf{K} = \frac{1}{3\tau}\sum_{i=1}^{3} \exp\left(-i\mathbf{Q}\cdot\mathbf{l}_i\right). \tag{5.10}$$

The value of $\mathbf{K}$ can be calculated from a single set of jump vectors,

$$\mathbf{l}_1 = \langle l, 0, 0\rangle \qquad \mathbf{l}_2 = \langle -l/2, -\sqrt{3}l/2, 0\rangle \qquad \mathbf{l}_3 = \langle -l/2, \sqrt{3}l/2, 0\rangle \tag{5.11}$$

and for a randomly oriented wavevector transfer $\mathbf{Q}$,

$$\mathbf{Q} = \langle Q\cos\phi\sin\theta, Q\sin\phi\sin\theta, Q\cos\theta\rangle. \tag{5.12}$$

We need to calculate the dot product for the three jump vectors,

$$\mathbf{Q}\cdot\mathbf{l}_1 = Ql\cos\phi\sin\theta \tag{5.13}$$

$$\mathbf{Q}\cdot\mathbf{l}_2 = -\tfrac{1}{2}Ql\cos\phi\sin\theta - \tfrac{\sqrt{3}}{2}Ql\sin\phi\sin\theta \tag{5.14}$$

$$\mathbf{Q}\cdot\mathbf{l}_3 = -\tfrac{1}{2}Ql\cos\phi\sin\theta + \tfrac{\sqrt{3}}{2}Ql\sin\phi\sin\theta. \tag{5.15}$$

To simplify notation, we substitute in the following expressions,

$$a = Ql\cos\phi\sin\theta \qquad b = \tfrac{\sqrt{3}}{2}Ql\sin\phi\sin\theta. \tag{5.16}$$

The dot products are now substituted into the exponentials in Eq. 5.10,

$$\exp\left(-i\mathbf{Q}\cdot\mathbf{l}_1\right) = \cos a - i\sin a \tag{5.17}$$

$$\exp\left(-i\mathbf{Q}\cdot\mathbf{l}_2\right) = \left[\cos\tfrac{a}{2} - i\sin\tfrac{a}{2}\right]\left[\cos b - i\sin b\right] \tag{5.18}$$

$$\exp\left(-i\mathbf{Q}\cdot\mathbf{l}_3\right) = \left[\cos\tfrac{a}{2} - i\sin\tfrac{a}{2}\right]\left[\cos b + i\sin b\right], \tag{5.19}$$

and the value of $\mathbf{K}$ is calculated,

$$\mathbf{K} = \frac{1}{3\tau}\sum_{i=1}^{3}\exp\left(-i\mathbf{Q}\cdot\mathbf{l}_i\right) = \frac{1}{3\tau}\left[\cos a + 2\cos\tfrac{a}{2}\cos b\right] - \frac{i}{3\tau}\left[\sin a + 2\sin\tfrac{a}{2}\cos b\right]. \tag{5.20}$$

We can now readily determine the magnitude and real part of $\mathbf{K}$,

$$|\mathbf{K}| = \frac{1}{3\tau}\left[1 + 4\cos^2 b + 4\cos b\cos\tfrac{3a}{2}\right]^{1/2} \tag{5.21}$$

$$\frac{\mathrm{Re}(\mathbf{K})}{|\mathbf{K}|} = \frac{\cos a + 2\cos\frac{a}{2}\cos b}{\left[1 + 4\cos^2 b + 4\cos b\cos\frac{3a}{2}\right]^{1/2}}. \tag{5.22}$$

This is the QENS function for a single-crystal honeycomb lattice. The $KC_{24}$ samples measured in this experiment are polycrystalline however, so it is necessary to take an orientational average over $\theta$ and $\phi$:

$$\langle S_{\mathrm{inc}}(Q,\omega)\rangle = \frac{1}{4\pi}\int_0^{2\pi}\int_0^{\pi}\left[S_{\mathrm{inc}}(\mathbf{Q},\omega)\right]\sin\theta\,\mathrm{d}\theta\mathrm{d}\phi. \tag{5.23}$$

To take into account a fraction of $H_2$ molecules which are not diffusing, we add a delta function[2] weighted by a $Q$-independent elastic-like factor ($f$). The experimentally measured scattering function is broadened by the instrumental resolution, $R(\omega)$. Therefore, the model

[2]It is not clear what the origin of the elastic-like intensity is, but from a practical point of view it is necessary to include the delta function to obtain good fits to the experimental data.

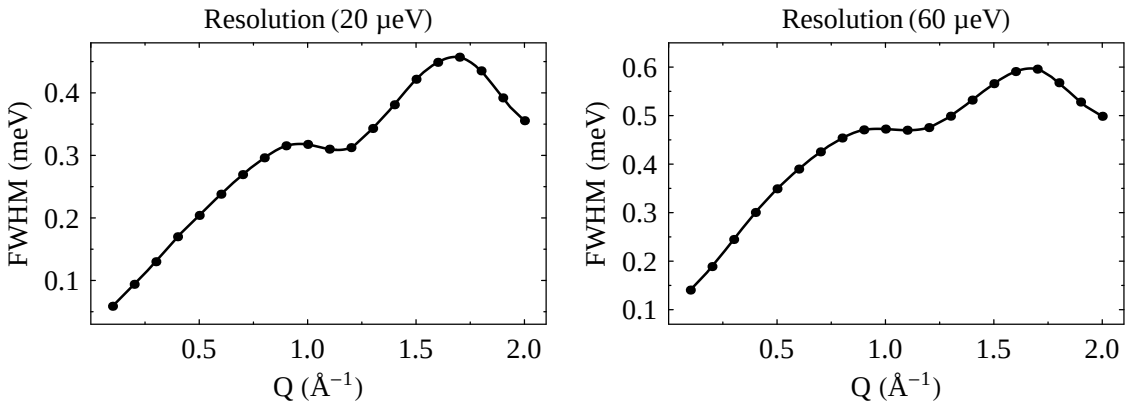


**Figure 5.4:** Linewidth (FWHM) of the honeycomb net model function $F(Q, \omega, \tau = 5\,\mathrm{ps}, l = 3.7\,\text{Å}, f = 0, A = 1)$ plotted versus momentum-transfer, $Q$. Resolution is a Lorentzian function with HWHM of 20 μeV (left) and 60 μeV (right).

function in its final form is obtained after taking the convolution of the powder-averaged honeycomb net model plus delta function with the instrument resolution,

$$F(Q, \omega, \tau, l, f, A) = A\left[(f)\delta(\omega) + (1-f)\langle S_{\mathrm{inc}}(Q, \omega)\rangle\right] * R(\omega) \tag{5.24}$$

$$= A\left[(f)R(\omega) + (1-f)\int_{-\infty}^{\infty} R(\omega - \omega')\langle S_{\mathrm{inc}}(Q, \omega)\rangle \mathrm{d}\omega'\right], \tag{5.25}$$

where $(Q, \omega)$ are variables and $(\tau, l, f, A)$ are the parameters to be fitted. For most of the fits, the jump distance $l$ was held fixed at the theoretical value of 3.7 Å. Several different jump distances were tested to determine whether they improved the fit. To simplify calculations, the resolution function was fitted to a sum of five Lorentzians and the convolution was carried out analytically before the orientational average. For the convolution of two Lorentzians the linewidths add linearly.

At finite instrument resolution, the linewidth of the honeycomb net model function $F(Q, \omega, \tau, l, f, A)$ varies with $Q$ in a distinct manner. This is illustrated in Fig. 5.4, where the line widths are plotted for $\tau = 5\,\mathrm{ps}$, $l = 3.7\,\text{Å}$, and $f = 0$ (equivalent to $D = 6.8 \times 10^{-9}\,\mathrm{m^2\,s^{-1}}$) at two different instrument resolutions. The sinusoidal character of the

curve begins to be damped out at coarser resolutions.

The QENS spectra of $KC_{24}(H_2)_{0.5}$ were fit simultaneously over all $Q$-values to the honeycomb net model function $F(Q, \omega, \tau, l, f, A)$ to optimize a single set of fit parameters $\{\tau,l,f\}$ for a given temperature. The amplitude $A$ was allowed to vary independently for each $Q$-value however. Fits for the 80 K to 110 K spectra using the theoretical $l = 3.7$ Å jump length are plotted in Figs. 5.5–5.8, respectively. Only the first ten momentum transfer groups are shown due to limited space.[3] The $y$-axes of the individual plots have a logarithmic scale to facilitate the visualization of the goodness-of-fit in both the peak regions and wing regions of the spectra. Fit parameters are summarized in Table 5.1.

In the 80 K spectra the wings are not well fitted by the model. For the higher temperature spectra, it is clear that the peak regions are not fitted well at larger $Q$-values. This can be fixed by allowing the elastic-like weighting parameter $f$ to vary with $Q$. The presence of a $Q$-dependent elastic-like intensity (sometimes called an EISF) usually indicates the presence of confined dynamics in the system. However there is no intuitive physical basis for such confined motion in $KC_{24}$ since the $H_2$ molecules are not chemically bonded or trapped within a rigid cage. Further, there is a large amount of correlation between the $\tau$ and $f$ parameters, which creates some doubt about the physical significance of the elastic-like intensity.

We must conclude that the honeycomb net jump diffusion model is not sufficient to fully describe the hydrogen dynamics in the $KC_{24}(H_2)_{0.5}$ system. There are a number of possibilities for this shortcoming. First, the model ignores the rotational motion of the $H_2$ molecules. Since $H_2$ has a large rotational constant, the characteristic frequencies are expected to be well above the range measured here. Nevertheless, there is expected to be

[3] The eleventh group has a momentum transfer of $Q = 1.74\,\text{Å}^{-1}$.

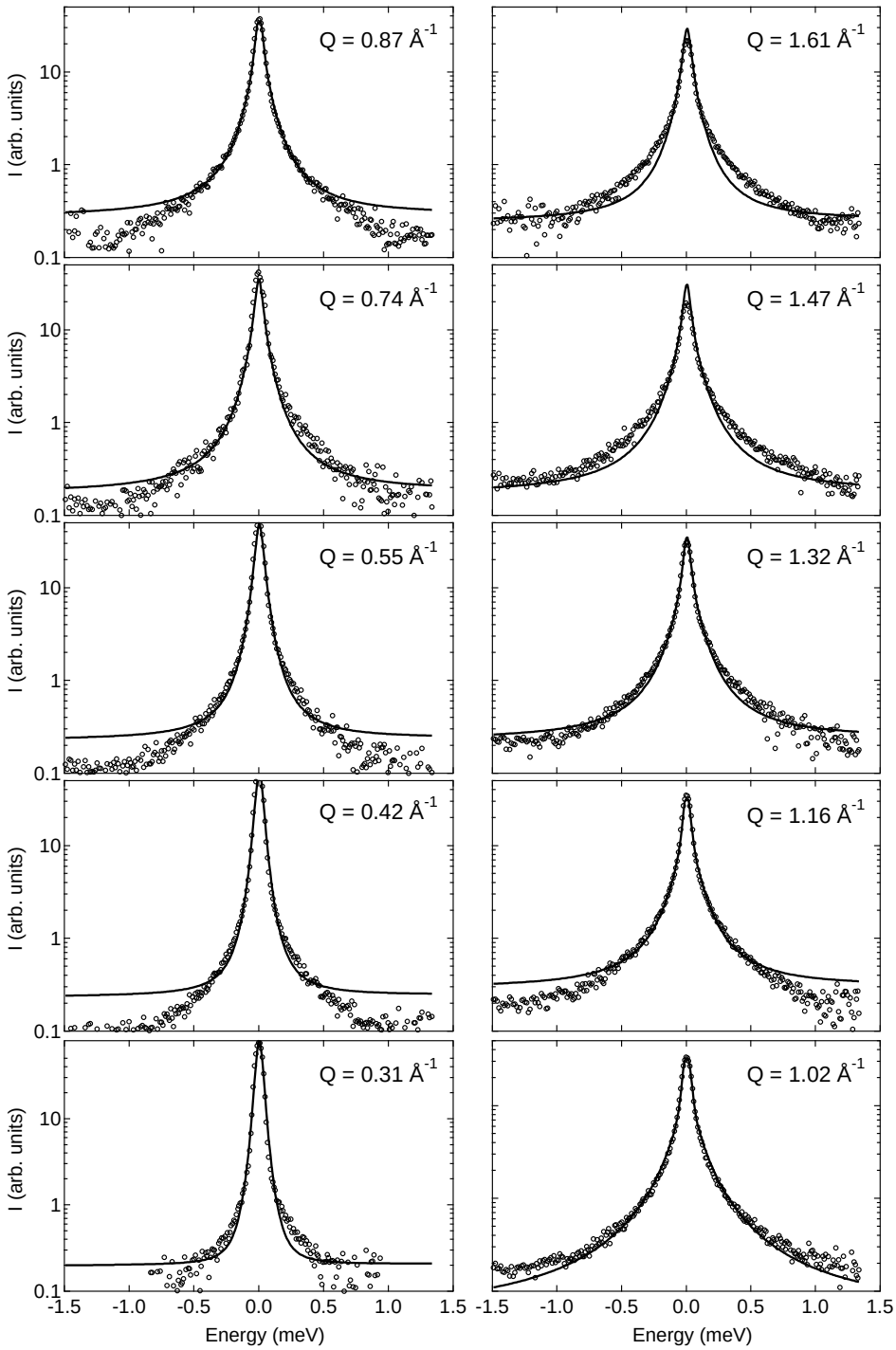


**Figure 5.5:** QENS spectra of $KC_{24}(H_2)_{0.5}$ at 80 K fitted to the honeycomb net jump diffusion model.

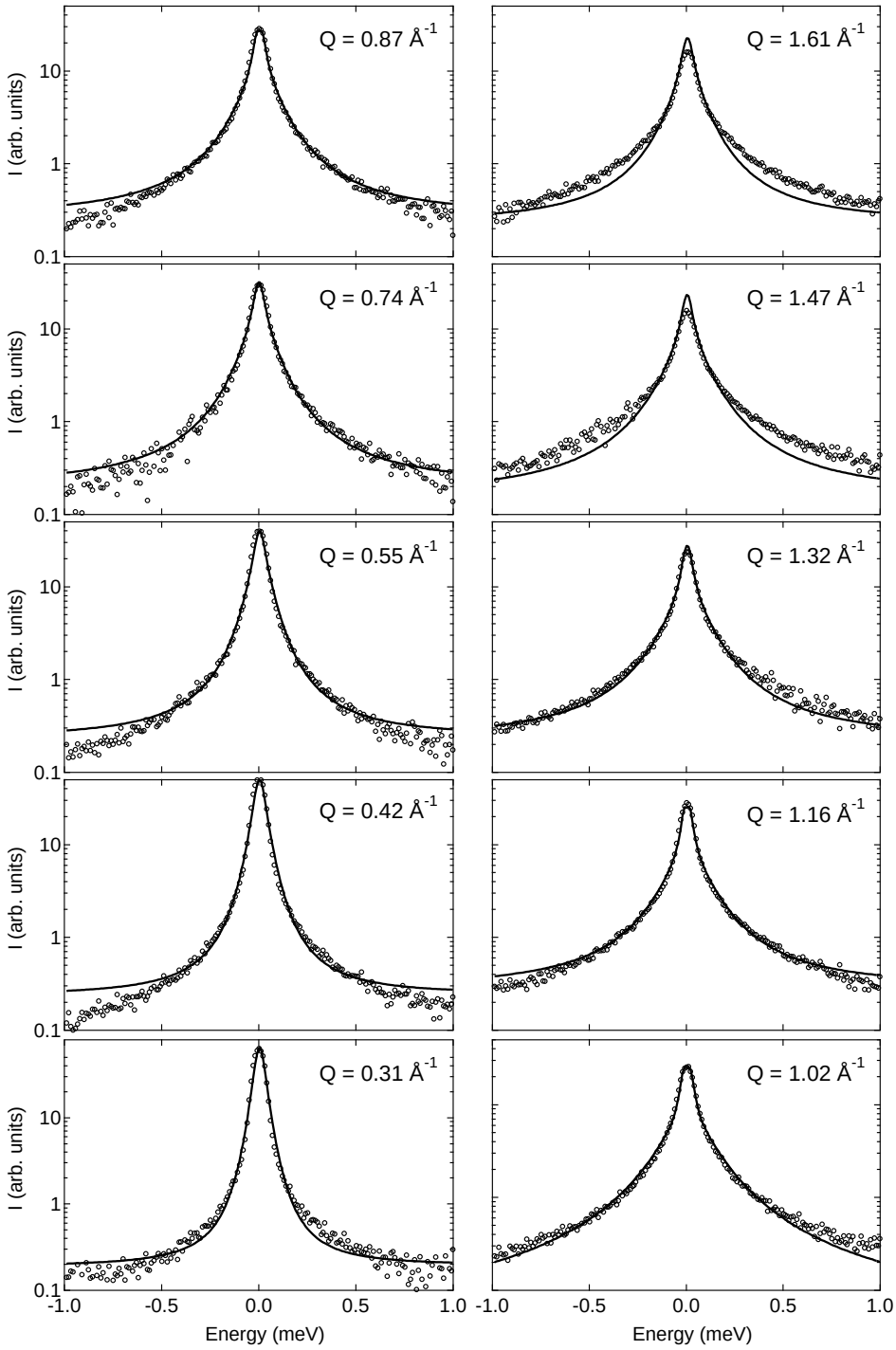


**Figure 5.6:** QENS spectra of $KC_{24}(H_2)_{0.5}$ at 90 K fitted to the honeycomb jump diffusion model. The reduced energy range of $\pm 1$ meV was used because fits to the full energy range of $\pm 1.5$ meV did not converge successfully.

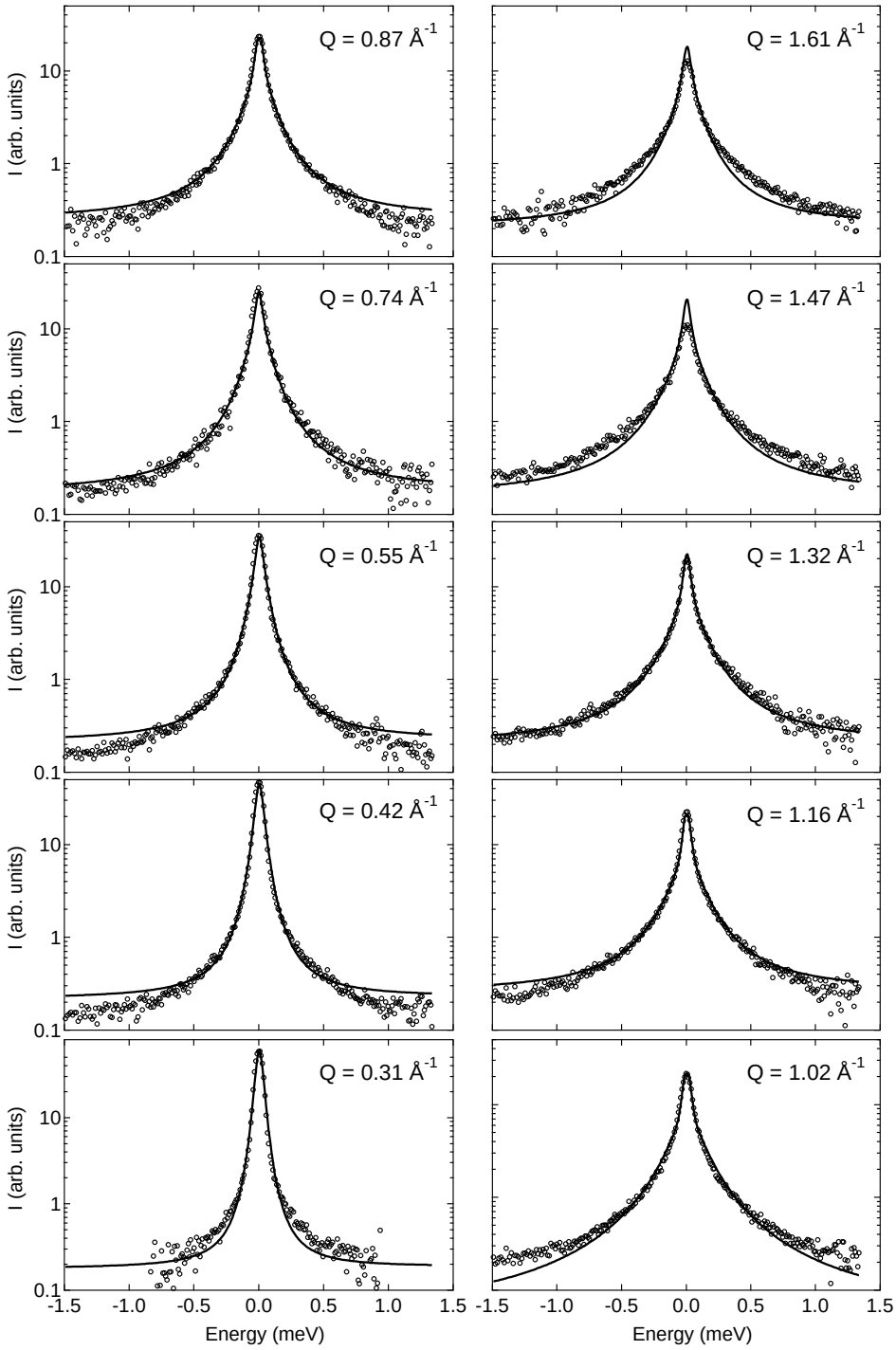


**Figure 5.7:** QENS spectra of $KC_{24}(H_2)_{0.5}$ at 100 K fitted to the honeycomb jump diffusion model.

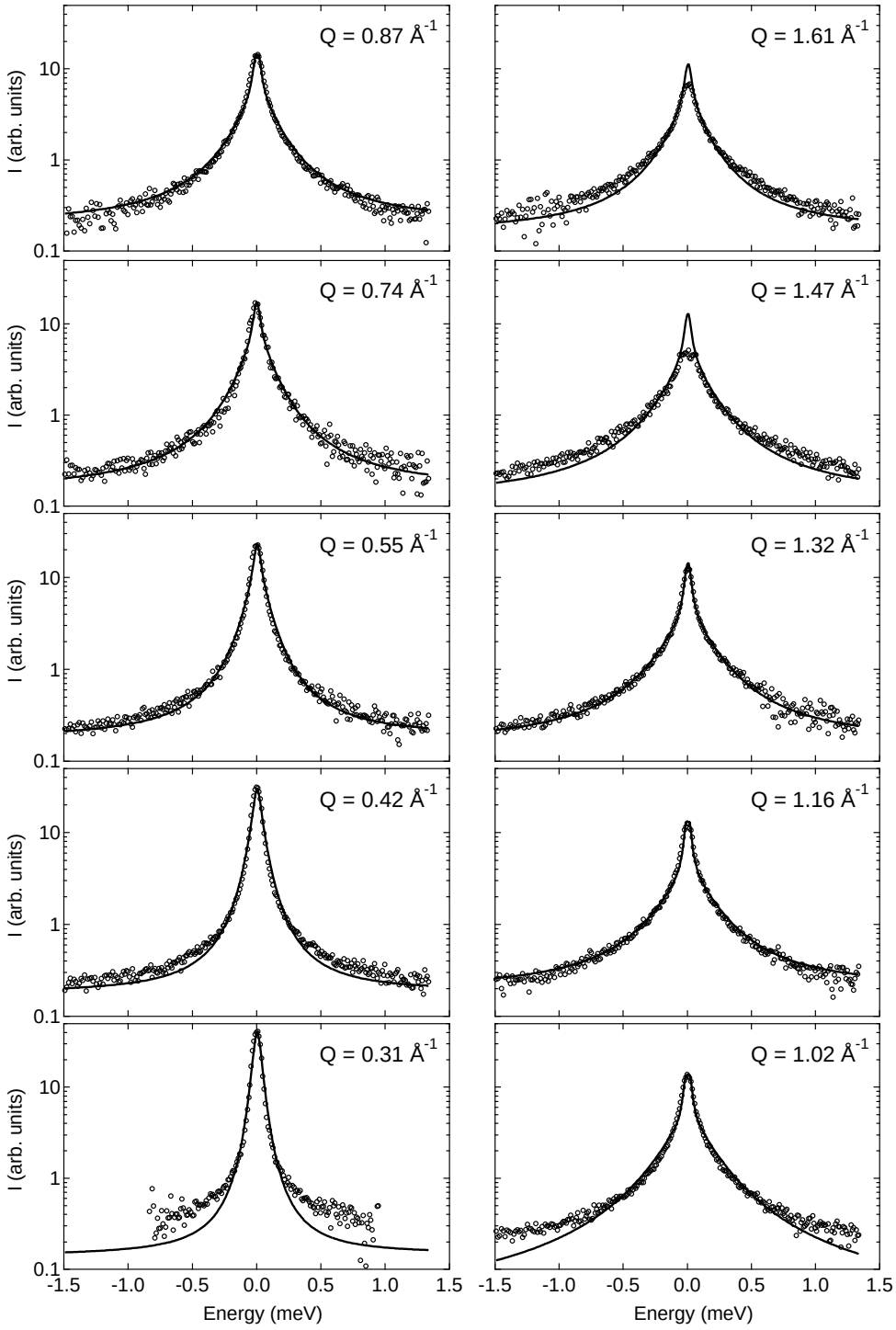


**Figure 5.8:** QENS spectra of $KC_{24}(H_2)_{0.5}$ at 110 K fitted to the honeycomb jump diffusion model.

**Table 5.1:** Honeycomb net jump diffusion model parameters from fits to the $KC_{24}(H_2)_{0.5}$ data

| Temperature (K) | $\tau$ (ps) | $l$ (Å)[a] | $f$ | $D$ ($10^{-9}$ m$^2$ s$^{-1}$)[b] |
|---|---|---|---|---|
| 80 | 10.36(4) | 3.7 | 0.214(2) | 3.30(1) |
| 90 | 7.80(2) | 3.7 | 0.167(1) | 4.39(1) |
| 100 | 6.38(2) | 3.7 | 0.146(1) | 5.36(2) |
| 110 | 4.29(1) | 3.7 | 0.126(1) | 7.98(3) |

[a] Jump length ($l$) was held fixed at 3.7 Å.
[b] The diffusion coefficient assumes two-dimensional translation.

some coupling between the rotational and translational dynamics which can affect peak shape. Second, it is probably incorrect to impose a single jump frequency on the diffusion process. As described later in the chapter, there are a wide range of jump frequencies present in the $KC_{24}(H_2)_{0.5}$ system. Developing a model with a *distribution* of jump frequencies is far from trivial, however. In the next section we use several "mechanism-independent" methods to estimate the diffusion coefficients and residence times of the $KC_{24}(H_2)_{0.5}$ system.

## 5.6 Estimates of diffusion coefficients

### 5.6.1 Low-$Q$ limit

In the limit of low $Q$, the honeycomb net jump diffusion model (Eq. 5.7) reduces to the expression for continuous two-dimensional diffusion (Eq. 5.2). Before fitting to data from polycrystalline samples, the orientational average must be calculated. The powder-averaged function can actually be determined analytically, as discussed by Lechner [90, 91]. The resulting expression is given by

$$\langle S_{\mathrm{inc}}(Q,\omega)\rangle = \frac{1}{8\pi k^3 DQ^2}\left(\frac{1+k^2}{\cos\alpha/2}\ln\frac{1+2k\cos\alpha/2+k^2}{1-2k\cos\alpha/2+k^2} + \frac{2\left(1-k^2\right)}{\sin\alpha/2}\arctan\frac{2k\sin\alpha/2}{k^2-1}\right), \quad (5.26)$$

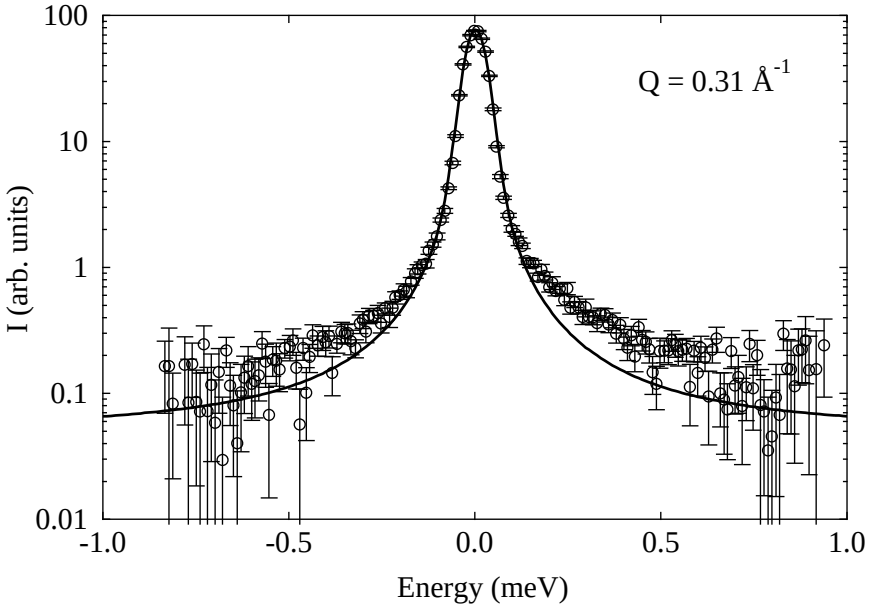


**Figure 5.9:** Experimental $KC_{24}(H_2)_{0.5}$ spectra measured at 110 K (with $Q = 0.31\,\text{Å}^{-1}$) fitted to the two-dimensional continuous diffusion model.

where the following terms need to be substituted in,

$$k = \left[1 + \left(\frac{\omega}{DQ^2}\right)^2\right]^{1/4} \qquad \sin\alpha/2 = \left(\frac{1-\cos\alpha}{2}\right)^{1/2} \tag{5.27}$$

$$\cos\alpha = \left[1 + \left(\frac{\omega}{DQ^2}\right)^2\right]^{-1/2} \qquad \cos\alpha/2 = \left(\frac{1+\cos\alpha}{2}\right)^{1/2} \tag{5.28}$$

This expression (Eq. 5.26) was fitted to experimental spectra at low $Q$. The fitted curve for the smallest momentum transfer group ($Q = 0.31\,\text{Å}^{-1}$) of the 110 K spectra is displayed in Fig. 5.9. From the fit parameters we obtain a two-dimensional self-diffusion coefficient of $D = 9.3(1) \times 10^{-9}\,\text{m}^2\,\text{s}^{-1}$. This is slightly larger than the self-diffusion coefficient of $7.8 \times 10^{-9}\,\text{m}^2\,\text{s}^{-1}$ obtained from the honeycomb net jump diffusion model. It can be seen in Fig. 5.9 that the goodness-of-fit in the wing regions is not sufficient. The chi-squared value for the fit was $\chi^2 = 7.8$. The values of the fitted parameter $D$ are summarized in Table 5.2 for all the temperatures.

**Table 5.2:** Comparison of the hydrogen self-diffusion coefficients for $KC_{24}(H_2)_{0.5}$ extracted from QENS data by fitting to different diffusion models

| | $D$ $(10^{-9}\ \mathrm{m^2\,s^{-1}})^a$ | | |
|---|---|---|---|
| Temperature (K) | Honeycomb[b] | Low-$Q$ limit[c] | High-$Q$ limit[d] |
| 80 | 3.30(1) | 2.16(4) | 5.9(3) |
| 90 | 4.39(1) | 5.42(3) | 6.2(3) |
| 100 | 5.36(2) | 6.53(4) | 6.7(4) |
| 110 | 7.98(3) | 9.29(7) | 7.5(4) |

[a] Self-diffusion coefficients are two-dimensional.
[b] Honeycomb net jump diffusion model.
[c] Two-dimensional continuous diffusion in the low-$Q$ limit.
[d] Geometry-independent jump diffusion in the high-$Q$ limit.

### 5.6.2 High-$Q$ limit

When Eq. 5.7 is averaged over large $Q$ values, the incoherent scattering function reduces to a Lorentzian with an average linewidth of $\langle\Gamma(Q)\rangle = 1/\tau$. In other words, the average quasielastic linewidth in the limit of large $Q$ is approximately independent of the geometry of the system and depends only on the the jump frequency. To estimate $\tau$, a resolution-broadened model function consisting of a Lorentzian function, a delta function, and a flat background was fitted to the experimental spectra. An example of fits to the five largest $Q$-values of the 110 K data is displayed in Fig. 5.10. Values of $\tau$ were obtained by averaging $\Gamma(Q)$ over the range $1.16\,\mathrm{Å}^{-1}$ to $1.74\,\mathrm{Å}^{-1}$. Residence times varied from 4.6 ps to 5.9 ps for the experimental temperatures. Two-dimensional self-diffusion coefficients were then calculated from the expression $D = l^2/4\tau$, using the jump length $l = 3.74\,\mathrm{Å}$. Values are summarized in Table 5.2. There is a modest discrepancy between the diffusion coefficients obtained from the rigorous honeycomb net model and from the approximate methods.

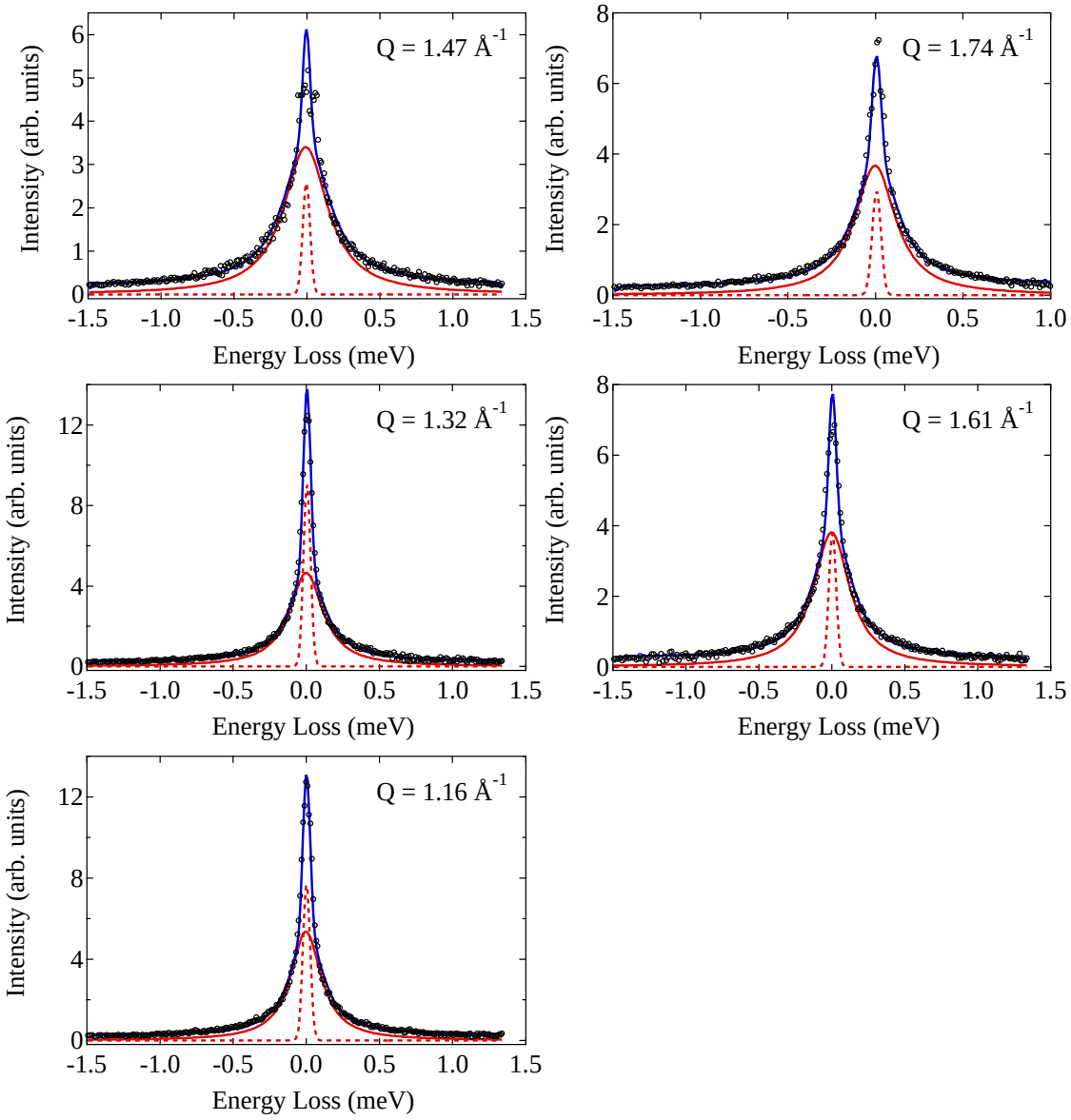


**Figure 5.10:** The five largest momentum-transfer groups of the QENS spectra at 110 K. Fitted curves: quasielastic (red, solid line), elastic (red, dashed line), and total (blue, solid line). The elastic line is the convolution of a delta function with instrument resolution. As illustrated, the quasielastic curve is a Lorentzian before convolution with resolution. The flat background is not shown.

### 5.6.3 Distribution of jump frequencies

The presence of more than a single jump frequency in the $KC_{24}(H_2)_{0.5}$ system is a highly intractable problem in the analysis and interpretation the QENS data. From data collected on a backscattering spectrometer (see Sec. 5.7), we know that there is also a slower diffusion process present in the $H_2/KC_{24}$ system with a residence time on the order of 100 to 1000 ps. This leads to the possibility that there are a *distribution* of diffusive jump frequencies. Incorporating such a frequency distribution into a rigorous jump diffusion model is problematic. Even for the simplest case of two hopping frequencies on a Bravais lattice, the resulting expression is too complicated to be fit to the QENS spectra from a two-dimensional, polycrystalline system.

The intermediate scattering function for unrestricted diffusion is a simple exponential decay, $I(\mathbf{Q},t) = \exp(-t/\tau)$, where $\tau$ is the characteristic relaxation time. This expression simply reflects how the system relaxes back to its equilibrium state after some external perturbation is switched off. If there are numerous hopping frequencies present in the system, however, we need to take a linear superposition of the exponential decays. This can be approximated by a *stretched* exponential,

$$I(Q,t) = \exp\left[-\left(\frac{t}{\tau}\right)^{\beta}\right], \tag{5.29}$$

where the stretching factor $\beta$ is taken to be between 0 and 1. This empirical relation is often referred to as the Kohlrausch-Williams-Watts (KWW) function. It describes a fairly broad distribution of relaxation times. The scattering function, $S(Q,\omega)$, is obtained by taking the Fourier transform of the KWW function.

The FT-KWW function was fitted to the QENS spectra of $KC_{24}(H_2)_{0.5}$ as a way of

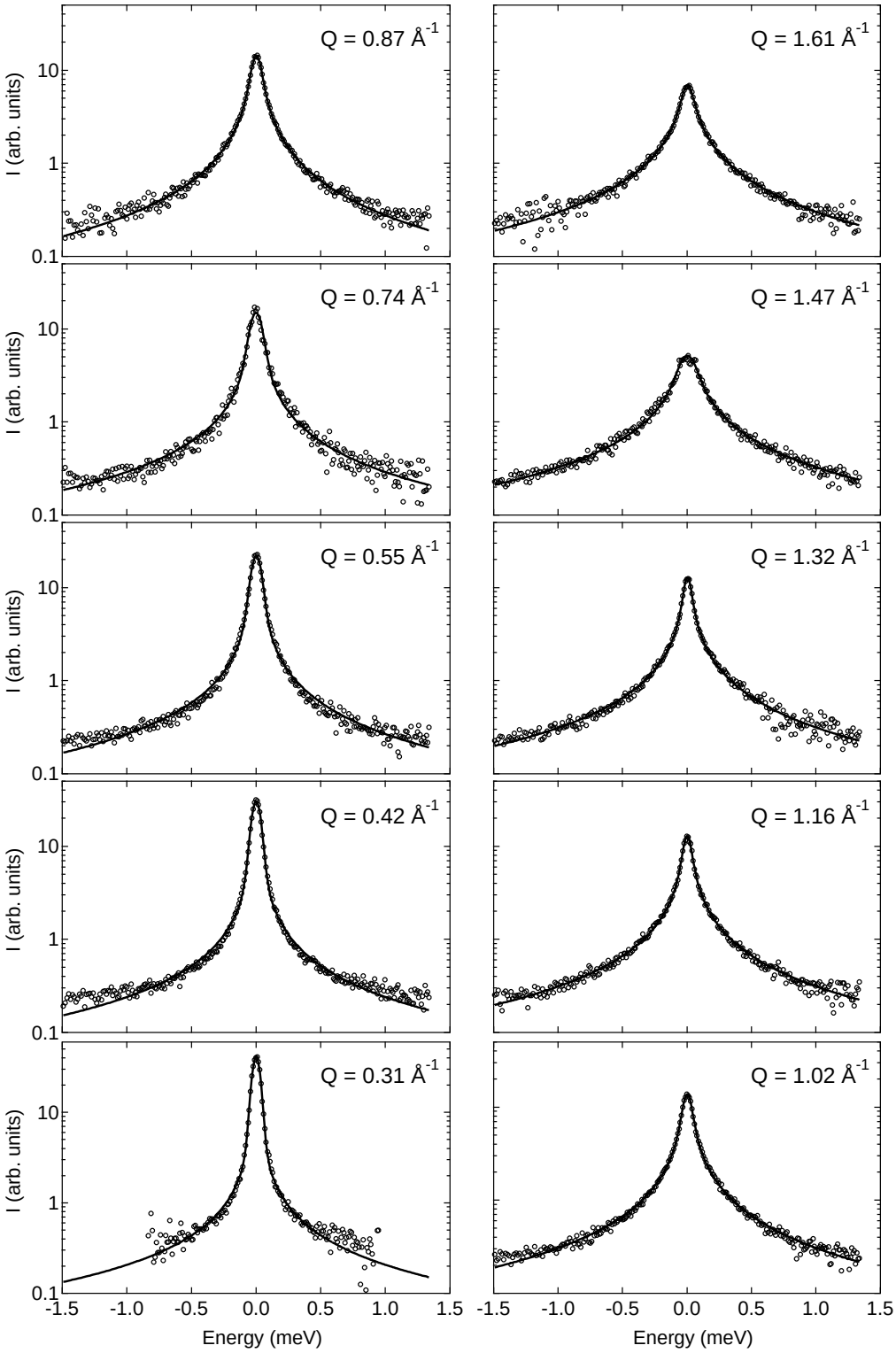


**Figure 5.11:** The QENS spectra of $KC_{24}(H_2)_{0.5}$ collected at 110 K, fitted to the FT-KWW function.

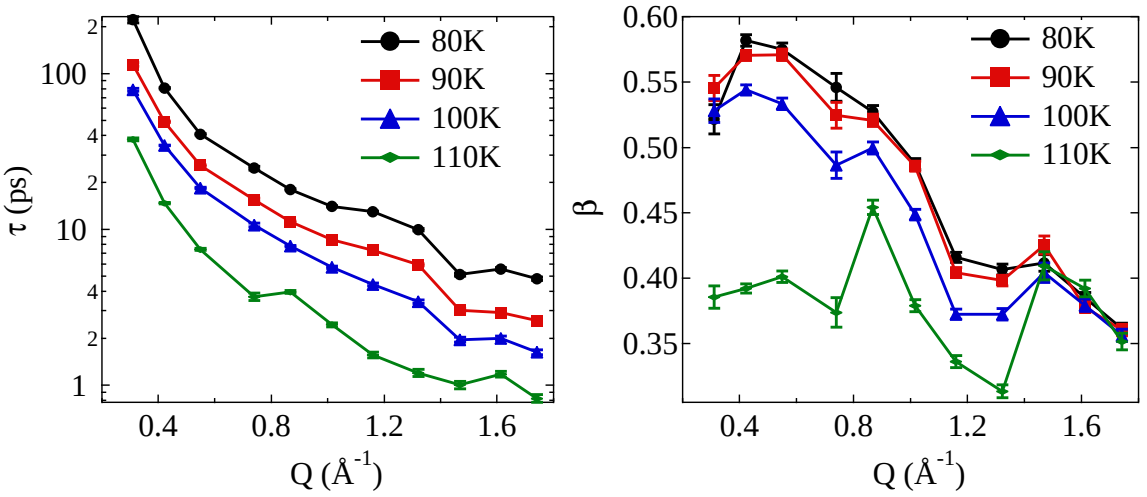


**Figure 5.12:** Parameters for the FT-KWW function fitted to the QENS spectra of $KC_{24}(H_2)_{0.5}$. Top: Best-fit values for $\tau$ as a function of momentum transfer. Bottom: Best-fit values for $\beta$ as a function of momentum transfer.

gauging the importance of multiple hopping frequencies on the $H_2$ dynamics. The detailed expression used for the fits is given by the LHS of the following equation,

$$\mathcal{F}\left[e^{-\left(\frac{t}{\tau}\right)^{\beta}} \times \mathcal{F}\left[Ae^{-\frac{\omega^2}{2\sigma^2}}\right]\right] = \mathcal{F}\left[e^{-\left(\frac{t}{\tau}\right)^{\beta}}\right] * Ae^{-\frac{\omega^2}{2\sigma^2}}, \tag{5.30}$$

where the Gaussian function is used to describe the instrument resolution.[4] The $\sigma$ parameters were determined by fits to the DCS resolution function and were held fixed during the fits. The convolution that appears on the RHS is due to the fact that the Fourier transform of a product equals the convolution of two individual Fourier transforms (i.e., convolution theorem). Also utilized is the fact that two successive Fourier transforms of a Gaussian yields the original Gaussian. During the least-squares fits, the outermost transform on the LHS was computed numerically. Fit parameters $\{\tau, \beta, A\}$ were allowed to vary independently in each momentum-transfer group. The resulting fits are shown in Fig. 5.11, and the fit parameters are summarized in Fig. 5.12. These are the best fits obtained so far, and

[4]The resolution function of the DCS instrument is well-described by a Gaussian function.

are certainly superior to those obtained for the honeycomb net jump diffusion model. Although the FT-KWW function is not a rigorous jump diffusion model, it can be considered a phenomenological indicator of the importance of a multiple hopping frequencies in the $KC_{24}(H_2)_{0.5}$ system.

## 5.7 Measurements at longer timescales

### 5.7.1 Overview

The high-flux backscattering spectrometer (HFBS)[5] located at NCNR has an energy resolution of better than 1 μeV [92]. This allows it to detect very slow dynamical processes with characteristic times from 100 ps to 10 ns, processes which are not resolvable on DCS. Measurements were collected on a $KC_{24}(H_2)_1$ system in order to verify whether there were slower $H_2$ hopping frequencies present.[6] For comparison, measurements on the same $KC_{24}(H_2)_1$ system were also performed on DCS over the same temperature range. The important finding from these measurements is that there are at least two distinct $H_2$ hopping frequencies in the $KC_{24}$ system.

### 5.7.2 Methods

The HFBS instrument was operated in both the fixed window and dynamic window modes. In the fixed window mode, the Doppler drive was stopped and only elastic scattering was recorded. A heating rate of $0.5\,\mathrm{K\,s^{-1}}$ was used for the temperature scan experiments and the total intensity was obtained by summing over all 16 detector banks. In the dynamic window

[5]The HFBS spectrometer is an indirect geometry instrument which utilizes the fact that the wavelength spread of a Bragg-diffracted neutron beam decreases as the scattering angle $2\theta$ approaches 180°. Incident energies of the neutrons are varied by the Doppler motion of the monochromator (i.e., controlled by a Doppler drive).

[6]Compared to other measurements, a larger hydrogen filling of $x = 1$ was used here, in order to improve the counting statistics on HFBS.

mode, the Si[111] crystal monochromator was operated at 24 Hz, providing a dynamic range of $\pm$ 17 μeV, a $Q$-range of 0.25 $\text{Å}^{-1}$ to 1.75 $\text{Å}^{-1}$, and an energy resolution of 0.85 μeV at the elastic peak.

### 5.7.3 Quasielastic scattering

QENS measurements were collected on the $KC_{24}(H_2)_1$ system using both the DCS and HFBS spectrometers. In Fig. 5.13a, the DCS spectra show resolution-limited elastic scattering at 40 K and quasielastic line broadening at higher temperatures. For the HFBS spectra illustrated in Fig. 5.13b, elastic scattering is dominant 45 K, while quasielastic broadening is significant at 55 K and 65 K. The combination of a sharp elastic-like component and broad quasielastic component is present in both the DCS and HFBS spectra. The peak intensity decreases with temperature, but in Fig. 5.13 the spectra have been scaled to equal height to facilitate comparison. Quasielastic broadening is present at the same temperature range in *both* the HFBS and DCS data. However the energy scales for the two spectra are vastly different. This means that there are at least two different hopping frequencies present in $KC_{24}(H_2)_1$. The characteristic residence times for these hopping motions were estimated from the high-$Q$ spectra (following the method discussed in Sec. 5.6.2) and are summarized in Table 5.3.

### 5.7.4 Elastic intensity

Using the fixed window mode of operation on HFBS, we measured the elastic intensity of the $H_2/KC_{24}$ system as a function of temperature. These scans are displayed in Fig. 5.14. The curve for $KC_{24}$ does not show any major changes between 4 K and 100 K. In contrast, the $KC_{24}(H_2)_1$ and $KC_{24}(H_2)_2$ curves show a rapid decrease in the elastic intensity starting at

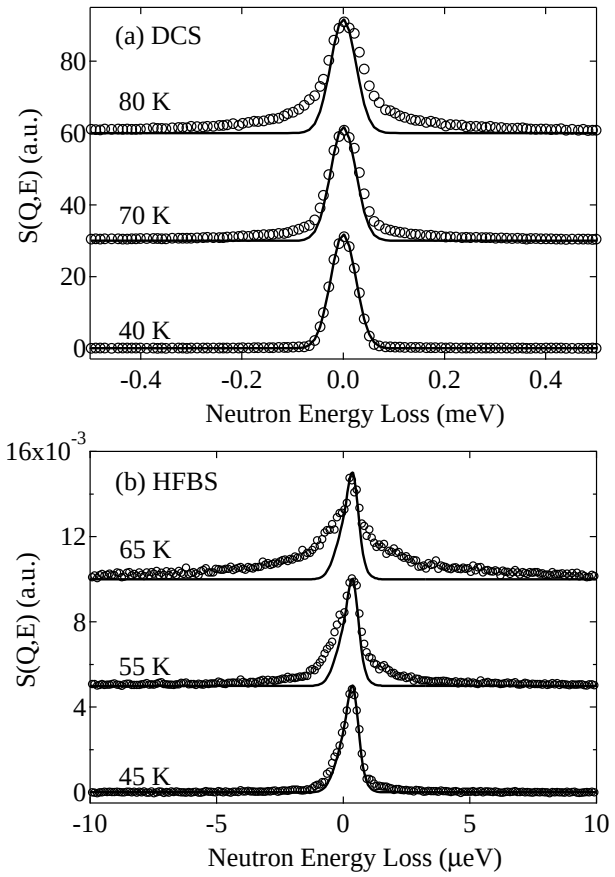


**Figure 5.13:** Quasielastic neutron scattering spectra of $KC_{24}(H_2)_1$: (a) from the DCS spectrometer, for the $Q = 1.84\,\text{Å}^{-1}$ group; (b) from the HFBS spectrometer, for the $Q = 0.87\,\text{Å}^{-1}$ group. The instrument resolution is included for comparison to the spectra at each temperature. The experimental spectra have been scaled to equal height, and offset for clarity.

**Table 5.3:** Residence times for thermally activated $H_2$ jump diffusion in $KC_{24}(H_2)_1$.

| DCS data[a] | | HFBS data[b] | |
|---|---|---|---|
| T (K) | $\tau$ (ps) | T (K) | $\tau$ (ps) |
| 60 | $13.4 \pm 0.2$ | 45 | $1330 \pm 36$ |
| 70 | $9.4 \pm 0.1$ | 55 | $699 \pm 12$ |
| 80 | $7.0 \pm 0.1$ | 65 | $372 \pm 7$ |

[a] Measurements on DCS probe the faster diffusion process.
[b] Measurements on HFBS probe the slower diffusion process.
[c] Residence times ($\tau$) were determined from the high-$Q$ limit, as described in Sec. 5.6.2.

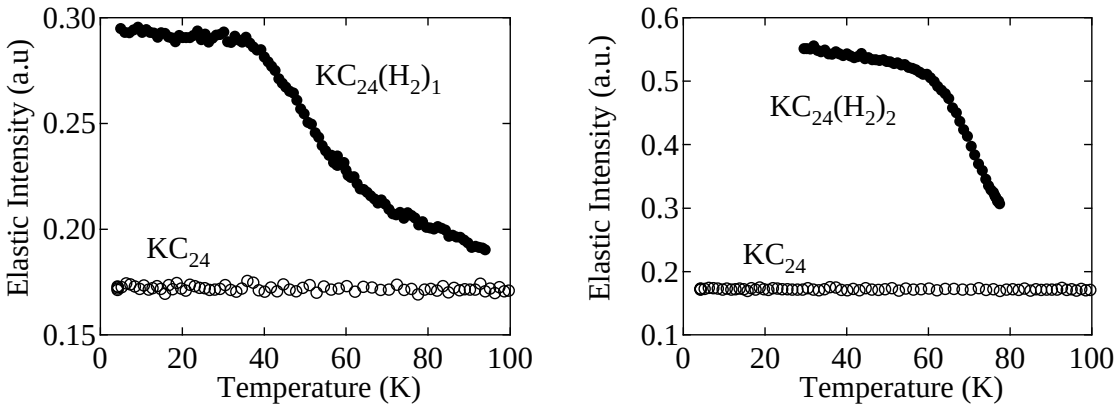


**Figure 5.14:** Elastic intensity from (left) $KC_{24}(H_2)_1$ and (right) $KC_{24}(H_2)_2$ as a function of temperature. Base intensity from $KC_{24}$ is also presented.

35 K and 60 K, respectively. The sudden drop in elastic signal is accompanied by the growth in quasielastic intensity (see Fig. 5.13), indicating the presence of hydrogen diffusion. Scans obtained from heating and cooling the sample at the same rate did not have any significant differences except that the $KC_{24}(H_2)_1$ heating curve was slightly more rounded near the transition point at 35 K compared to the cooling curve.

One possibility that needed to be ruled out was that desorption of $H_2$ could also contribute to the decrease in elastic scattering at higher temperatures. For the composition $KC_{24}(H_2)_1$ this is unlikely because the equilibrium pressure at 60 K is close to 0 kPa, and the decrease begins at an even lower temperature of 35 K. Nevertheless, to be certain that the elastic intensity was not affected by $H_2$ desorption, we monitored the equilibrium pressure with a high resolution manometer over the entire temperature scan. We are confident that the concentration of adsorbed $H_2$ did not change significantly over the measured temperature range, and would not have contributed to the large decrease in the elastic intensity.

## 5.8 Molecular dynamics simulations

### 5.8.1 Computational details

To better understand the hydrogen diffusion mechanism in $KC_{24}$, molecular dynamics simulations were performed and compared with the experimental results. The theoretical $\left(\sqrt{7} \times \sqrt{7}\right)$ structure with stoichiometry $KC_{28}$ was used for all simulations. To reduce the size of the supercell, the structure consisted of two graphite layers and one potassium metal layer in a A|A stacking sequence with an interlayer spacing of 5.69 Å for the intercalated layer and 3.35 Å for the unintercalated layer. The relaxed supercell was contained within a simulation box with parameters $a = 51.9837$ Å, $b = 45.0192$ Å, and $c = 9.04$ Å. Periodic boundary conditions were enforced. The host graphite structure was held constant in all simulations. For the 1:1 $H_2$:K ratio, the supercell had the stoichiometry $K_{64}C_{1792}(H_2)_{64}$, which consists of 64 unit cells.[7]

The program GULP V.3.4 was used as the computational engine for the simulation [93]. Forcefields were taken directly from the literature without further optimization. Hydrogen molecules were treated as Lennard-Jones spheres, which ignores the fact that they are quantum rotors. Because the dimensions of the $KC_{24}$ system are on the order of the hydrogen de Broglie wavelength, it is necessary to account for quantum effects in the simulations. This is done using the Feynman-Hibbs (FH) variational approach. A quantum particle of mass $m$ is represented by a Gaussian with a width $\sqrt{\beta\hbar^2/12\mu}$ that accounts for the spread in position due to the uncertainty principle [24]. The quantum partition function of $N$

[7] The $KC_{24}(H_2)_1$ stoichiometry was used in order to increase the number of hydrogens in the supercell, thereby increasing the quality of the calculated mean-squared-displacement and the intermediate scattering function.

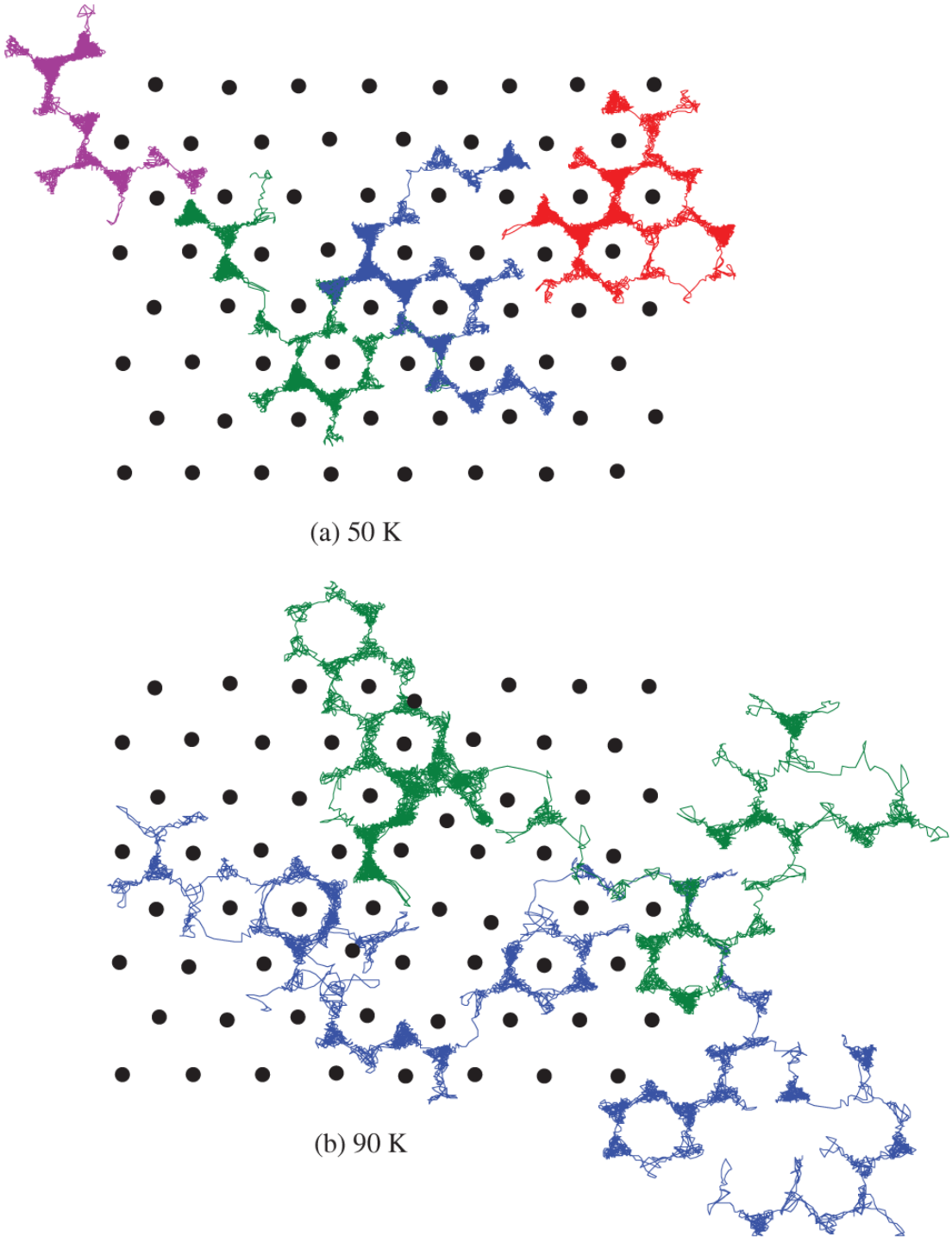


**Figure 5.15:** Molecular dynamics trajectories of hydrogen particles in $KC_{24}$ at (top) 50 K and (bottom) 90 K. Total simulation time is 500 ps for each trajectory. Trajectories of four different particles are shown for 50 K while trajectories of two particles are shown for 90 K. Individual trajectories are identified by the color of the traces. Black circles indicate the final positions of potassium atoms. Carbon atoms are not shown.

particles is

$$Z = \frac{1}{N!}\left(\frac{m}{2\pi\beta\hbar^2}\right)^{3N/2}\int\cdots\int dr_1\ldots dr_N \exp\left[-\beta\sum_{i<j}U_{\mathrm{FH}}(r_{ij})\right] \tag{5.31}$$

where $\beta = 1/k_{\mathrm{B}}T$ and

$$U_{\mathrm{FH}}(r) = \left(\frac{6\mu}{\pi\beta\hbar^2}\right)^{3/2}\int U(|r+R|)\exp\left(-\frac{6\mu}{\beta\hbar^2}R^2\right)dR. \tag{5.32}$$

Here $U_{\mathrm{FH}}(r)$ is the effective potential between a pair of molecules with reduced mass $\mu$. The integral in Eq. 5.31 is difficult to evaluate. As described in Ref. [24], the term $U(|r+R|)$ is expanded around $r$ to the fourth order in $R$ to obtain a more tractable expression. This approximation to the FH potential was incorporated into all of the molecular dynamics simulations. The carbon and potassium potentials were extracted from Ref. [94], which were based on empirical fits to lattice parameters, elastic moduli, and infrared-Raman data for graphite and potassium-intercalated graphite. The hydrogen potentials were taken from Ref. [24] in which they successfully reproduced bulk hydrogen data. The forcefield has a tapered 12.0 Å cutoff. Since intercalate layers are separated by a distance of 9.04 Å, this means that interlayer interactions in the simulation are very weak. Simulations were run using an NVT ensemble with a leapfrog-verlet integrator and a time-step of 1 fs. Temperature was controlled with a Nose-Hoover thermostat. Simulations were equilibrated for 50 ps (50 000 steps), followed by a production run of 500 ps (500 000 steps).

### 5.8.2 Results

Molecular dynamics trajectories of $KC_{24}(H_2)_1$ were run at temperatures of 30 K, 40 K, 50 K, 70 K, and 90 K. Sample $H_2$ trajectories are illustrated in Fig. 5.15 for the 50 K and 90 K

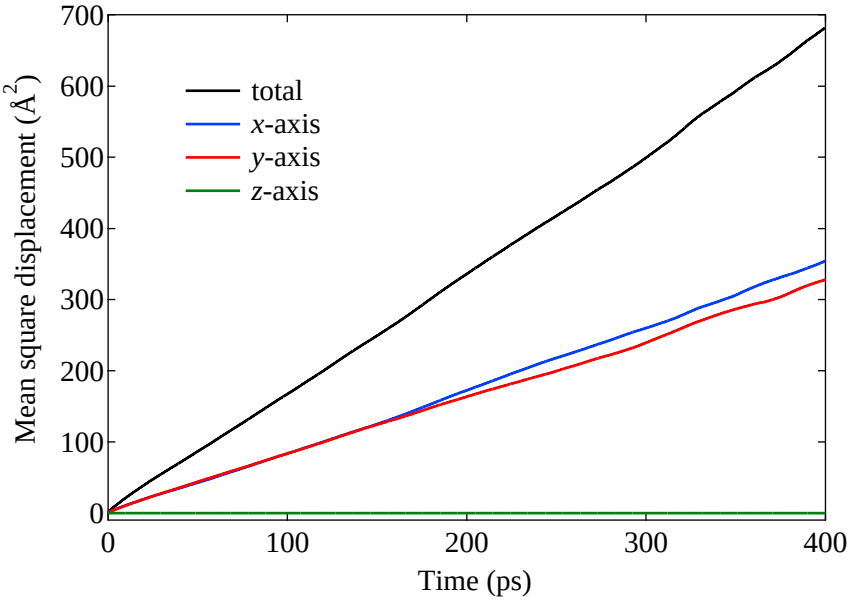


**Figure 5.16:** Total mean square displacement of $H_2$ particles in $KC_{24}(H_2)_1$ at 70 K. The projections of the MSD along the $x$-axis, $y$-axis, and $z$-axis of the simulation box are also shown.

simulations. Each single-colored trace depicts the trajectory of a single $H_2$ particle for a 500 ps production run. As can be seen in the trajectories, hydrogens rattle around inside of the triangular cages formed from three potassium atoms for extended periods of time before jumping into a neighboring triangular site. As expected for thermally activated diffusion, the jump frequency appears to be much larger at 90 K than at 50 K. In a jump diffusion model, it is assumed that the particle vibrates around its equilibrium position between jumps. This vibrational motion can be decoupled from the diffusive motion and distilled into a separate Debye-Waller factor. For the $KC_{24}(H_2)$ system, however, the particles seem to jump rapidly between three local energy minima within the triangular sites (evident in the triangular shaped motifs present in Fig. 5.15). The potassium atoms do not diffuse at the temperatures investigated here, but mainly vibrate around their equilibrium positions (though several potassiums did actually jump to neighboring graphite hexagons during the 90 K run).

Dynamical properties were calculated from $H_2$ trajectories using the nMOLDYN package [95]. The mean square displacement (MSD), with respect to a particular axis $\mathbf{n}$, is calculated for a system of $N$ particles with the expression,

$$\Delta^2(t) = \frac{1}{N}\sum_{i=1}^{N}\left[\mathbf{n}\cdot(\mathbf{R}_i(t) - \mathbf{R}_i(0))\right]^2. \tag{5.33}$$

For illustration, the MSD of $H_2$ at 70 K is plotted in Fig. 5.16. As expected, the diffusion is two-dimensional and the MSD along the $z$-axis is zero. The sum of the $x$-projection and $y$-projection give the total MSD. We calculate the 2D self-diffusion coefficient from the slope of the MSD in the long-time limit, using the Einstein relation

$$\lim_{t\to\infty}\Delta^2(t) = 4Dt. \tag{5.34}$$

In Fig. 5.17 the simulated self-diffusion coefficients are plotted with the experimental diffusion coefficients (calculated from the DCS residence times listed in Table 5.3). Agreement between the experimental and simulated self-diffusivities is remarkably good, especially considering that the MD forcefields were used without optimization. The fact that simulated values are larger than than experimental values might be due to the FH corrections, which have the overall effect of increasing the hydrogen mobility. The fact that such excellent agreement is obtained with experimental data with an unoptimized forcefield perhaps indicates that the layered geometry, not the fine form of the intermolecular potentials, is the main determining factor in the dynamics.

Between 40 K and 90 K, the simulated diffusivities follow the expected Arrhenius relation

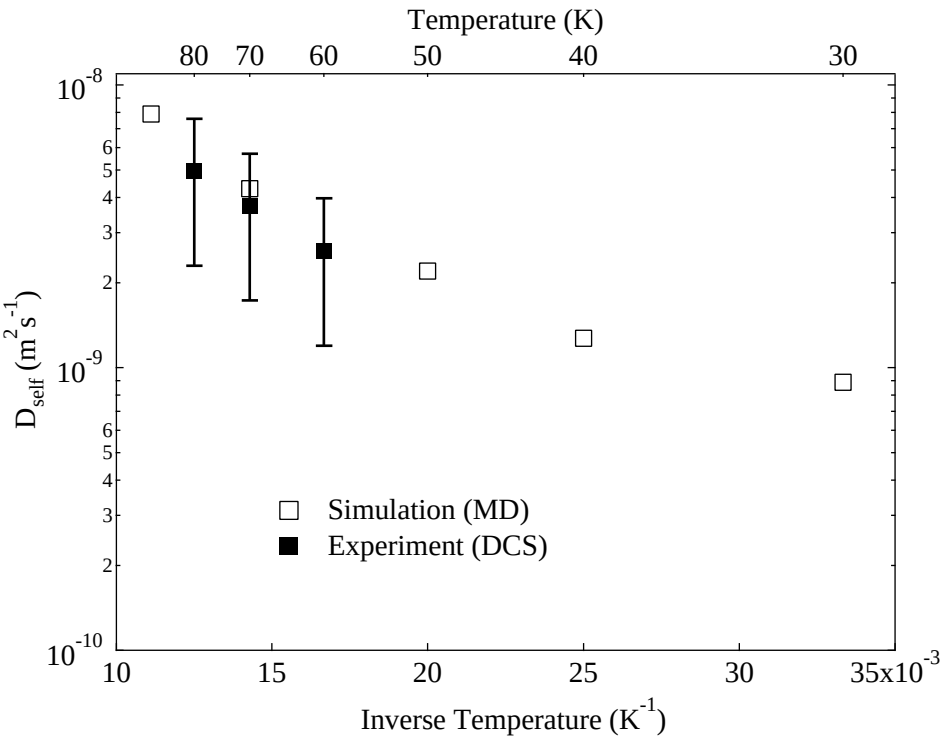


**Figure 5.17:** Comparison of self-diffusion coefficients of $H_2$ in $KC_{24}(H_2)_1$ obtained from experiment and from MD simulation. Experimental self-diffusivities were obtained from QENS data collected on the DCS instrument.

for a thermally activated process,

$$D = D_0 \exp\left(-\frac{E_\mathrm{a}}{T}\right), \tag{5.35}$$

where $D$ is the self-diffusion coefficient, $D_0$ is the pre-factor, and $E_\mathrm{a}$ is the activation coefficient. For experimental diffusivities we obtain values of $D_0 = 3.43 \times 10^{-8}\,\mathrm{m^2\,s^{-1}}$ and $E_\mathrm{a} = 155\,\mathrm{K}$. For the simulated self-diffusivities the values are $D_0 = 2.99 \times 10^{-8}\,\mathrm{m^2\,s^{-1}}$ and $E_\mathrm{a} = 128\,\mathrm{K}$.

### 5.8.3 Concentration effects

The jump diffusion model is only valid in the dilute limit where site-blocking and correlation are absent (see Section 5.2.4). In other words, at large $H_2$ concentrations we cannot apply

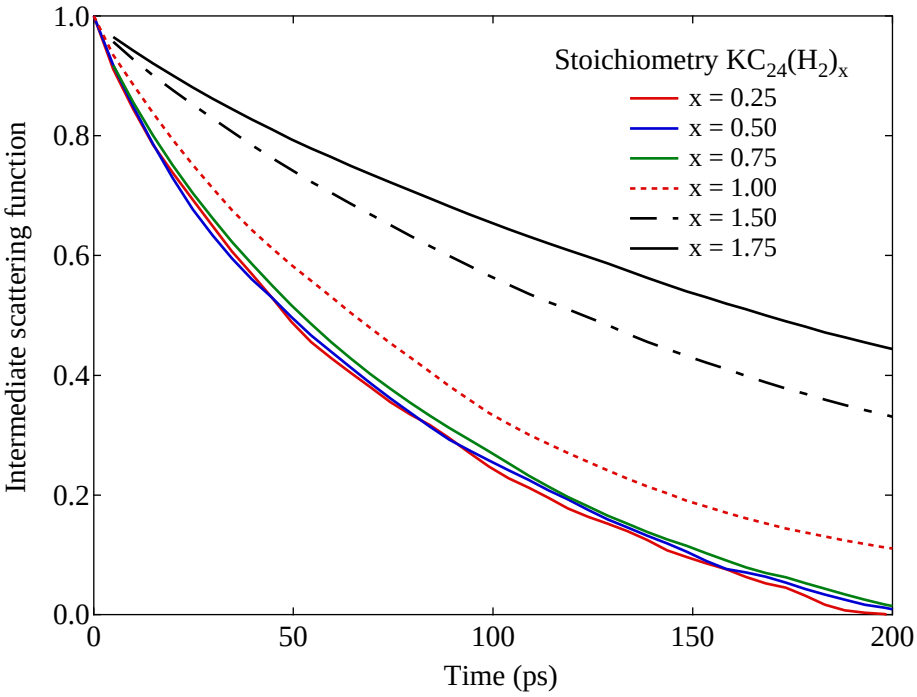


**Figure 5.18:** Intermediate scattering function at $Q = 1.0\,\text{Å}^{-1}$ calculated from MD trajectories of hydrogen in the theoretical $KC_{28}(H_2)_1$ structure. Changes in the ISF with concentration indicate site-blocking and correlation effects on the line shape.

a jump diffusion model to obtain a meaningful diffusion coefficient. In fact, the lineshape itself might not be well-described by the jump diffusion model at large concentrations. Therefore it is best to remain in the dilute-limit where the correlation between successive jumps is negligible and the diffusivity only needs to be corrected for site-blocking. To test whether the dilute-limit approximation can be applied to the experimental QENS data, MD simulations were performed at 90 K for various $H_2$ fillings. Computational details were otherwise the same as the previous simulations.

For direct comparison of line shapes it was convenient to calculate the incoherent intermediate scattering function,

$$I_{\text{inc}}(\mathbf{Q},t) = \frac{1}{N}\sum_{i}^{N}\sigma_{\text{inc},i}^{2}\langle \exp\left[-i\mathbf{Q}\cdot\mathbf{R}_i(0)\right]\exp\left[i\mathbf{Q}\cdot\mathbf{R}_i(t)\right]\rangle, \tag{5.36}$$

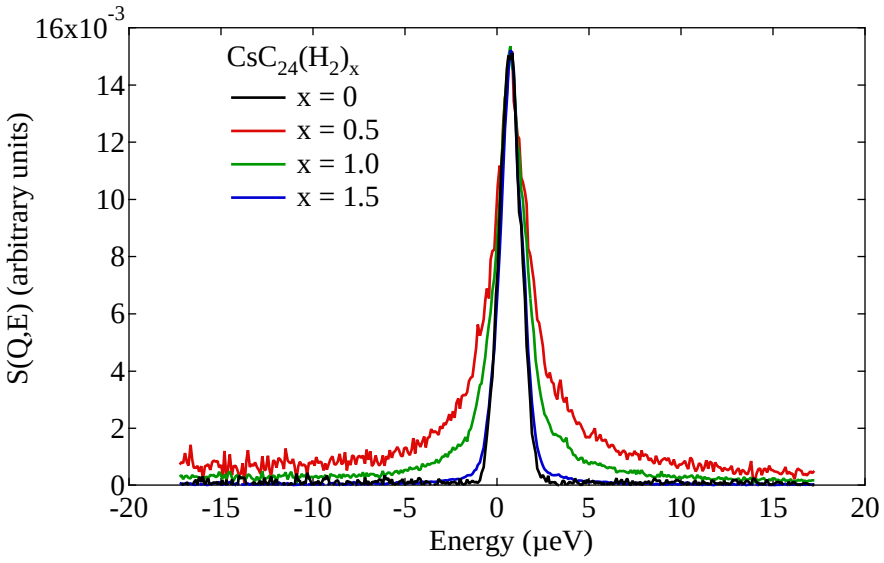


**Figure 5.19:** QENS spectra at 65 K collected on HFBS for three different hydrogen fillings in $CsC_{24}$. The background signal from $CsC_{24}$ at 4 K is also displayed. Spectra are scaled to equal height.

which describes correlation between the initial position and the final position. In unrestricted translational diffusion, $I_{\text{inc}}(\mathbf{Q}, t)$ should decay to zero at infinite time. Powder-averaged ISFs were calculated from the MD trajectories at $Q = 1.0\,\text{Å}^{-1}$. They are plotted in Fig. 5.18. The effect of correlations on the line shape becomes noticeable above at a stoichiometry of $x = 1.0$. Therefore, it seems that the dilute-limit approximation is not valid for $x > 1$. However, the dilute-limit approximation at $x = 0.5$ (for which most QENS measurements were collected) is clearly sufficient. Concentration effects on hydrogen diffusion in a $CsC_{24}(H_2)_x$ sample were investigated experimentally on the HFBS instrument.[8] Spectra were collected at three different hydrogen loadings and are shown in Fig. 5.19. It is clear that the breadth of the quasielastic peak decreases at large concentrations.

[8]It would have been better to have collected data on a $KC_{24}$ sample rather than a $CsC_{24}$ sample. On a qualitative level, though, concentration effects should be similar in both systems.

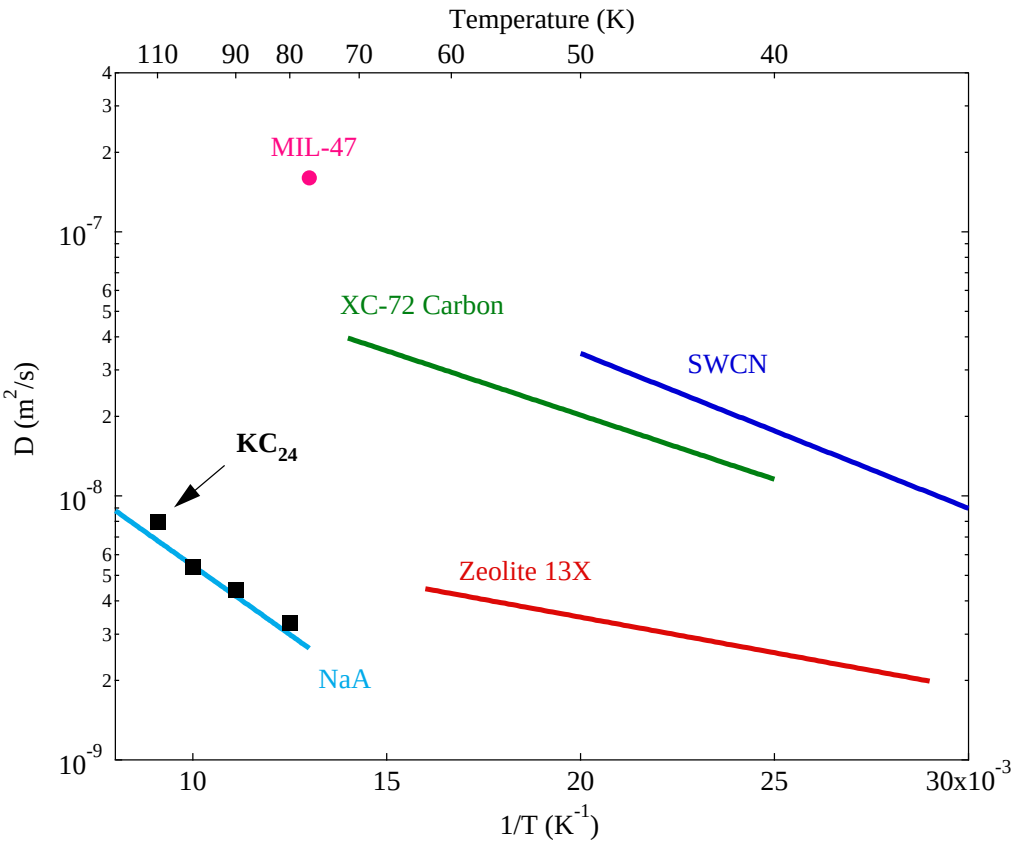


**Figure 5.20:** Comparison of hydrogen diffusivity in a variety of adsorbents. Hydrogen self-diffusion coefficients in $KC_{24}$ are plotted as black squares. Values for single-walled carbon nanotubes (SWCN) and a carbon black material (XC-72) are illustrated. Data is also included for a type A zeolite (NaA), a type X zeolite (13X), and a metal-organic framework (MIL-47).

## 5.9 Discussion

### 5.9.1 Comparison with carbons, zeolites, and MOFs

In Fig. 5.20 the hydrogen diffusivity[9] in $KC_{24}$ is plotted as a series of solid black squares, and is compared to values for single-walled carbon nanotubes [96] and the carbon black XC-72 [97]. Also plotted are self-diffusion coefficients for the type-A zeolite NaA [98], the type-X zeolite 13X [99], and the metal-organic framework MIL-47 [100]. It should be noted that the self-diffusion coefficients for $KC_{24}$ are two-dimensional, and should actually be multiplied by a factor of 2/3 for direct comparison to three-dimensional systems.

[9]Extracted from fits of the honeycomb net jump diffusion model to the QENS spectra of $KC_{24}(H_2)_{0.5}$.

Hydrogen diffusivity in $KC_{24}$ is more than an order-of-magnitude slower than in other carbon sorbents. It is similar in magnitude to diffusivities in the microporous zeolites (13X and NaA). Both $KC_{24}$ and the 13X/NaA zeolites share a nanoporous geometry. Hydrogen diffuses in $KC_{24}$ through narrow channels formed between closely spaced graphene layers. Similarly, diffusion in NaA and 13X occurs though intra-crystalline channels with molecular-sized windows. The widths of these cavities are on the order of the $H_2$ molecule diameter. For example, the windows of NaA have a van der Waals diameter of about $\sigma \approx 2.9\,\text{Å}$, while the interlayer separation of $KC_{24}(H_2)_{0.5}$ has a van der Waals diameter of $\sigma \approx 2.3\,\text{Å}$. The narrow intra-crystalline channels of $KC_{24}$, and of zeolites NaA and 13X, act as steric barriers that slow down the diffusion considerably. Interestingly, the steric barriers are also reflected in the molecular-sieve properties of these materials. In comparison, hydrogen diffuses mostly on the outer surfaces of carbon blacks and SWCNs, subject to fewer steric diffusion barriers. Geometry appears to be a dominant factor in determining the diffusion properties of hydrogen adsorbed in porous materials, while the actual chemical identity of the sorbent material appears to be of secondary importance.

### 5.9.2 Diffusion on two time-scales

A puzzling feature of the QENS data for $KC_{24}(H_2)_1$ is that it shows diffusion processes occurring on two distinct time scales (see Table. 5.3). The extremely slow diffusivity measured on HFBS is fairly unique and cannot be easily explained with a simple jump diffusion model. This type of slow diffusion (detectable on a backscattering spectrometer) is sometimes observed in metal hydrides and is typically attributed to H trapping at strong attractive sites. The origin of trapping sites in $KC_{24}$ is not clear however. Dual timescales in certain metal hydrides have also been linked to the simultaneous presence of fast, localized motions

between closely spaced interstitial sites and slower, long-range diffusion [101]. Similarly, elastic-like features in the QENS spectra of $H_2$/sorbent systems are usually explained in terms of a slow-diffusing population of hydrogen molecules [96, 99, 102].

One possible explanation is that the fast process originates from rapid individual jumps of the $H_2$ molecules while the slow process originates from in-plane jumps of the potassiums. Hydrogen molecules tend to cluster around the potassiums due to both electrostatic and dispersion interactions. When a potassium atom jumps, the fast-moving $H_2$ molecules quickly reconfigure around the new site of the potassium atom. This fluctuation in $H_2$ particle density can be detected by the backscattering spectrometer as slow diffusion. An alternative theory can be developed by hypothesizing that the adsorbed hydrogen forms a new phase. Lateral interactions between the adsorbed hydrogens may cause them to coalesce into tightly packed islands. Molecules in the interior of an island will have less mobility than the molecules at the island periphery. Measurements on a completely filled $KC_{24}(H_2)_2$ composition would provide some indirect information on the $H_2$ diffusivity in a tightly packed arrangement. The possibilities of phase transformations in the $H_2$ adsorbate will be discussed further in the next subsection.

### 5.9.3 Phase transformations

For a system consisting of $H_2$ monolayers on a clean graphite surface, transitions between commensurate and incommensurate solid 2D phases are determined by a competition between the hydrogen-hydrogen interactions and the hydrogen-surface interactions. At low $H_2$ concentrations, interactions with the periodic graphite corrugation potential are dominant, resulting in a commensurate, solid-like adsorbate phase [103]. As the surface coverage is increased and the lateral interactions between hydrogen molecules grow more important,

the commensurate solid monolayer becomes unstable relative to the formation of long-range dislocations, leading to a domain-wall intermediate phase [104]. In the Kosterlitz-Thouless theory of two-dimensional phase transformations, this type of intermediate phase is sometimes called a hexatic phase [105–107]. It is unique to two-dimensional systems and does not occur for three-dimensional systems. Diffusion along the fluid-like domain wall boundaries is considerably faster than within the domain interior [108]. This can result in the two time-scales for the system diffusivity. If the temperature is increased, an isotropic two-dimensional liquid is eventually formed. For the $H_2$/graphite system this transition occurs at around 20 K.

We studied the phase behavior of the $H_2/KC_{24}$ system by measuring the elastic intensity as a function of temperature (see Fig. 5.14). There is a distinct drop in elastic intensity starting at around 35 K which exceeds the expected decrease from the Debye-Waller factor. This is due to the onset of $H_2$ diffusion within the measurable time window of the instrument. However, the decrease in intensity with further heating is gradual, not abrupt. This means that there is no discrete $H_2$ melting transition in $KC_{24}$ such as is observed for $H_2$ on a graphite surface. Instead, there is a gradual increase in hydrogen mobility with temperature. The corrugated potential of the host $KC_{24}$ is dominant compared to the lateral interactions between hydrogen molecules. What occurs, therefore, is a gradual thermally-induced increase in diffusion through a solid-like sublattice, rather than a distinct solid-to-fluid bulk phase transition.

Bulk $H_2$ melts at a temperature of around 14 K. Confinement of $H_2$ in a porous material is known in some cases to lower the freezing temperature. For $H_2$ in Vycor, a porous glass with cavities of ∼60 Å, the freezing temperature has been measured at 8 K. In the smaller pores (∼20 Å) of the silica glass MCM-48, though, the melting temperature is little

changed from the bulk value of 14 K [109]. The strong binding interactions between $H_2$ and $KC_{24}$ appear to have the opposite effect on the "melting" behavior.[10] Hydrogen diffusivity (within the instrument time window) in $KC_{24}(H_2)_1$ is not detected until a temperature of 35 K, considerably higher than the bulk melting point. However there is not enough information to determine whether this actually is a phase transition. To make more conclusive observations of the phase behavior in the $H_2/KC_{24}$ system, other experimental techniques such as calorimetry or diffraction should be utilized.

## 5.10 Conclusions

Hydrogen self-diffusion in $KC_{24}$ was studied with QENS measurements and with MD simulations. The diffusivity in $KC_{24}$ is over an order of magnitude smaller than in other carbon adsorbents. It appears that steric diffusion barriers from the molecular-sized pore dimensions of $KC_{24}$ are the main factors in slowing down the diffusion. The hydrogen self-diffusion coefficients follow the Arrhenius relation for a thermally activated process. Good agreement is observed between the experimental and simulated diffusivities in $KC_{24}$ without optimization of the forcefields, hinting once again that geometry is the significant factor. Experimental quasielastic scattering was observed from an extremely slow process ($\tau \sim 1000$ ps) and a faster process ($\tau \sim 10$ ps). The origin of the slow process is still unclear. There was no sharp melting transition in $KC_{24}(H_2)_1$, but rather a gradual increase in $H_2$ mobility with temperature.

[10] Since most measurements were collected above the critical temperature of hydrogen, it may not be accurate to denote this as melting.